Fully Lagrangian Modeling of MEMS With Thin Plates

Srinivas Telukunta, *Student Member, IEEE, ASME, Student Member*, and Subrata Mukherjee, *ASME, Fellow*

***Abstract*—Microelectromechanical systems (MEMS) sometimes use beam or plate shaped conductors that can be very thin—with $h/L \approx \mathcal{O}(10^{-2}-10^{-3})$ (in terms of the thickness h and length L of the side of a square pate). Such MEMS devices find applications in microsensors, microactuators, microjets, microspeakers and other systems where the conducting plates or beams oscillate at very high frequencies. Conventional boundary element method (BEM) analysis of the electric field in a region exterior to such thin conductors can become difficult to carry out accurately and efficiently especially since MEMS analysis requires computation of charge densities (and then surface tractions) separately on the top and bottom surfaces of such plates. A new boundary integral equation (BIE) is proposed to handle the computation of charge densities for such high aspect ratio geometries. In the current work, this has been coupled with finite element method (FEM) to obtain the response behavior of devices made of such high aspect ratio structural members. This coupling of electrical and mechanical problem is carried out using a Newton scheme based on a Lagrangian description of both the mechanical and electrical domains. [1603]**

***Index Terms*—Aspect ratio, boundary element method (BEM), boundary integral equations, microelectromechanical systems (MEMS), nearly singular integrals, Newton scheme, relaxation scheme, singular integrals, small gap, thin plates, thin shells.**

I. Introduction

THE field of microelectromechanical systems (MEMS) is a very broad one that includes fixed or moving microstructures; encompassing microelectromechanical, microfluidic, microelectrofluidic-mechanical, microoptoelectromechanical, and microthermal-mechanical devices and systems. MEMS usually consists of released microstructures that are suspended and anchored, or captured by a hub-cap structure and set into motion by mechanical, electrical, thermal, acoustical, or photonic energy source(s).

Typical MEMS structures consist of arrays of thin beams with cross sections in the order of microns $(\mu\mathrm{m})$ and lengths in the order of ten to hundreds of microns (see, for example, Fig. 1). Sometimes, MEMS structural elements are plates. An example is a small rectangular silicon plate with sides in the order of mm and thickness of the order of microns, that deforms when subjected to electric fields. Owing to its small size, significant forces and/or deformations can be obtained with the application of low voltages (≈10 V). Examples of devices that utilize vibrations of such plates are comb drives (see Fig. 1), synthetic microjets ([2], [3]—for chemical mixing, cooling of electronic components, micropropulsion, turbulence control, and other macro flow properties), microspeakers [4], etc. Schematic of such a microjet, based on microelectrofluidic-mechanical systems, is shown in Fig. 2.

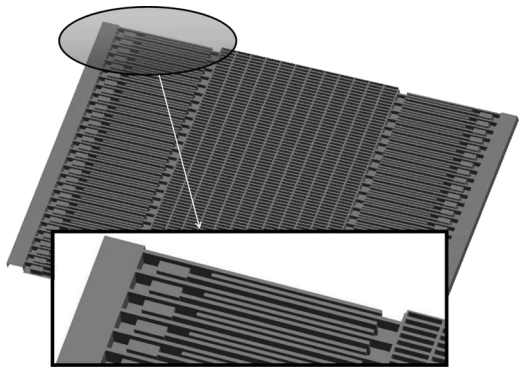

Fig. 1. Parallel plate resonator: geometry and detail of the parallel plate fingers (form [1]).

Numerical simulation of electrically actuated MEMS devices have been carried out for around a decade or so by using the boundary element method (BEM—see, e.g., [5]–[9]) to model the exterior electric field and the finite element method (FEM—see, e.g., [10]–[12]) to model deformation of the structure. The commercial software package MEMCAD [13], for example, uses the commercial FEM software package ABAQUS for mechanical analysis, together with a BEM code FastCap [14] for the electric field analysis. Other examples of such work are [15]–[17]; as well as [13], [18] for dynamic analysis of MEMS.

The focus of this paper is the study of quasi-static response behavior of MEMS devices made up of very thin conducting plates. This requires BEM analysis of the electric field exterior to these thin conducting plates. A convenient way to model such a problem is to assume plates with vanishing thickness and solve for sum of the charges on the upper and lower surfaces of each plate [19]. The standard boundary integral equation (BIE) with a weakly singular kernel is used here and this approach works well for determining, for example, the capacitance of a parallel plate capacitor. For MEMS calculations, however, one must obtain the charge densities separately on the upper and lower surfaces of a plate since the traction at a surface point on a plate depends on the square of the charge density at that point. The gradient BIE is employed in [20] to obtain these charge densities separately. The formulation given in [20] is a BEM scheme

Manuscript received May 18, 2005; revised November 14, 2005 and January 19, 2006. This work was supported in part by Grants EEC-0303674 and CMS-0508466 of the National Science Foundation to Cornell University. The work of S. Telukunta was supported by the Sibley School of Mechanical and Aerospace Engineering, Cornell University. Subject Editor N. Aluru.

S. Telukunta is with the Sibley School of Mechanical and Aerospace Engineering, Upson Hall, Cornell University, Ithaca, NY 14853 USA.

S. Mukherjee is with the Department of Theoretical and Applied Mechanics and Sibley School of Mechanical and Aerospace Engineering, Kimball Hall, Cornell University, Ithaca, NY 14853 USA (e-mail: Sm85@cornell.edu).

Digital Object Identifier 10.1109/JMEMS.2007.878891

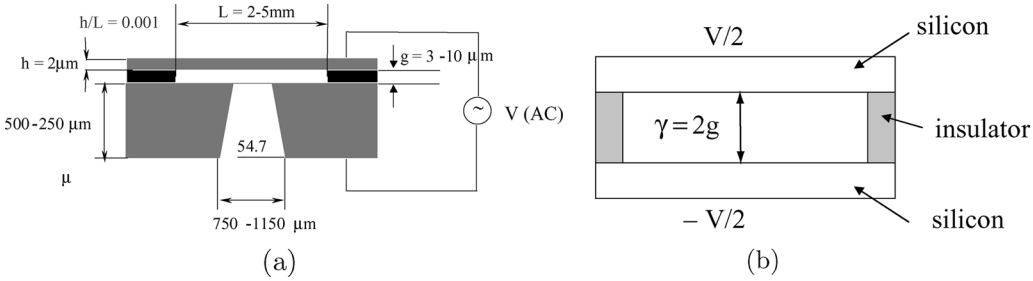

Fig. 2. (a) Schematic of a synthetic microjet. (b) Simulation model of a synthetic microjet.

that is particularly well suited for MEMS analysis of very thin plates—for $h/L \leq .001$—in terms of the length L (of a side of a square plate) and its thickness h. A similar approach can also be developed for MEMS and nanoelectromechanical systems (NEMS) with very thin beams [21]. Similar work has also been reported recently by Chen *et al.* [22] in the context of determining fringing fields and levitating forces for 2-D beam shaped conductors in MEMS combdrives.

The coupled BEM/FEM methods employed in the references aforecited perform a mechanical analysis on the undeformed configuration of a structure (Lagrangian approach) and an electrical analysis on the deformed configuration (Eulerian approach). A relaxation method is then used for self-consistency between the two domains. Therefore, the geometry of the structure must be updated before an electrical analysis is performed during each relaxation iteration. This procedure increases computational effort and introduces additional numerical errors since the deformed geometry must be computed at every stage. Li and Aluru [23] first proposed a Lagrangian approach for the electrical analysis as well, thus obviating the need to carry out calculations based on the deformed shapes of a structure. Two- and three-dimensional (2-D and 3-D) quasi-static Lagrangian exterior BEM analysis was addressed in [23] and [24]; while a fully coupled 2-D quasi-static MEMS analysis has been carried out in [25]. A fully-coupled 2-D dynamic Lagrangian MEMS analysis has been recently carried out by De and Aluru [26]. Additional advantages of the fully Lagrangian approach, for dynamic analysis of MEMS, are described in [26], in which a Newton method has been developed and compared with the relaxation scheme. A fully coupled Lagrangian (quasi-static) BEM/FEM analysis, but with the standard (not thin plate) BEM, is presented in [27].

The primary contributions of the present work are as follows. First, a coupled BEM-FEM analysis is presented in which the MEMS plate elements are thin and packed relatively close together. The exterior BEM analysis is 3-D while the FEM analysis allows for moderately large nonlinear deformation of the elastic plates. A fully Lagrangian formulation is presented for both the mechanical and electrical analyses. This includes a Lagrangian formulation (new) for the gradient BIE that is needed to obtain the separate charges on the top and bottom faces of a thin conducting plate. Finally, a Newton scheme, analogous to that in [26], is developed for the present problem. Results from the Newton scheme are compared with those from an iterative relaxation scheme.

This paper is organized as follows. The usual and gradient BIEs for potential theory, in an infinite region exterior to a structure composed of thin conducting plates, are first presented and regularized. This is then formulated in a total Lagrangian scheme. Next, a finite element scheme for deformation analysis of a plate is presented. This is followed by a description of a relaxation and a Newton scheme for coupling the electrical and mechanical problems. Finally, numerical results are presented and discussed for the model problem of a parallel plate capacitor (to simulate a microjet response behavior). A discussion section completes the paper. Finally, it is important to realize that the actual problem of simulating a microjet involves dynamics, as well as coupling the electromechanical problem with microfluidics. The present paper, however, is only a step in that direction and the effect of fluid forces is ignored in this work. A start has been made in modeling of damping forces in MEMS with thin plates [28]. Future research calls for fully coupling fluids forces in BEM/FEM MEMS modeling and analysis.

II. Electrical Problem in the Exterior Domain

Fig. 3 shows (as an example of a MEMS device) a deformable, clamped plate over a fixed ground plane. The undeformed configuration is B with boundary ∂B. The plate deforms when a potential V is applied between the two conductors, and the deformed configuration is called b with boundary ∂b. The charge redistributes on the surface of the deformed plate, thereby changing the electrical force on it and this causes the plate to deform further. A self-consistent final state is reached, and this state is computed in the present work by both the relaxation and Newton schemes.

A. Electric Field BIEs in a Simply Connected Body

First consider the solution of Laplace's equation in a 3-D simply connected body.

1) Usual BIE—Indirect Formulation: Referring to Fig. 4, for a source point $\boldsymbol{\xi} \in B$ (with bounding surface ∂B), one has the usual indirect BIE

$$\phi(\boldsymbol{\xi}) = \int_{\partial B} \frac{\nu(\mathbf{y})}{4\pi r(\boldsymbol{\xi}, \mathbf{y})\epsilon} ds(\mathbf{y}) \tag{1}$$

where $\mathbf{y}$ is a field point, ϕ is the potential, $\mathbf{r}(\boldsymbol{\xi}, \mathbf{y}) = \mathbf{y} - \boldsymbol{\xi}$, $r = |\mathbf{r}|$, ϵ is the dielectric constant of the medium, ds is the area of

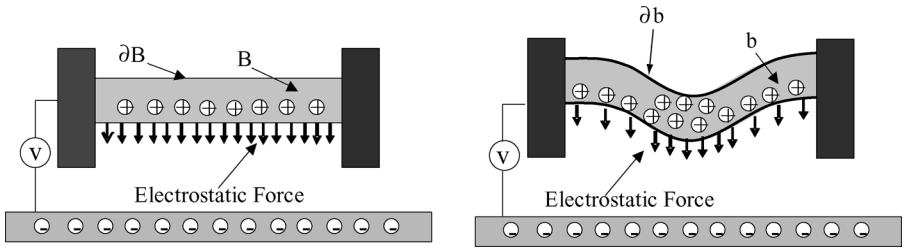

Fig. 3. A deformable clamped plate over a fixed ground plane.

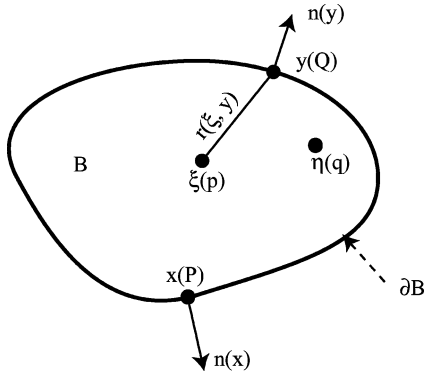

Fig. 4. Notation used in boundary integral equations.

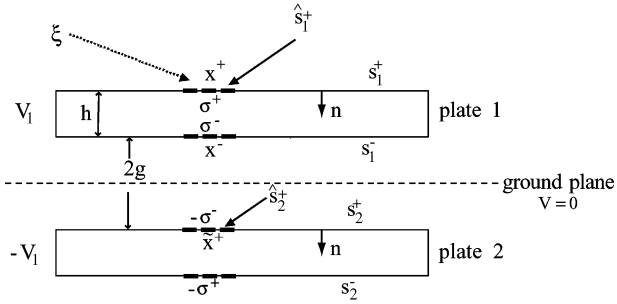

Fig. 5. Parallel plate capacitor with two plates.

an infinitesimal surface element on ∂B and ν is the (unknown) surface density function on ∂B.

2) Gradient BIE—Indirect Formulation: Taking the gradient of ϕ at the source point $\boldsymbol{\xi}$ results in:

$$\nabla_{\boldsymbol{\xi}}\phi(\boldsymbol{\xi}) = \int_{\partial B} \frac{\nu(\mathbf{y})}{4\pi\epsilon}\nabla_{\boldsymbol{\xi}}\left(\frac{1}{r(\boldsymbol{\xi},\mathbf{y})}\right) ds(\mathbf{y}) = \int_{\partial B} \frac{\nu(\mathbf{y})\mathbf{r}(\boldsymbol{\xi},\mathbf{y})}{4\pi r^3(\boldsymbol{\xi},\mathbf{y})\epsilon} ds(\mathbf{y}) \quad (2)$$

Alternatively, one can write (2) as:

$$\frac{\partial\phi}{\partial\xi_k}(\boldsymbol{\xi}) = \int_{\partial B} \frac{\nu(\mathbf{y})(y_k - \xi_k)}{4\pi r^3(\boldsymbol{\xi},\mathbf{y})\epsilon} ds(\mathbf{y}) \quad (3)$$

Note that, in general, the function $\nu(\mathbf{y})$ is not the charge density. It becomes equal to the charge density when B is the infinite region exterior to the conductors. This is discussed in Section II-B.

B. BIES in Infinite Region Containing Two Thin Conducting Plates

Now consider the situation shown in Fig. 5. Of interest is the solution of the following Dirichlet problem for Laplace's equation

$$\nabla^2\phi(\mathbf{x}) = 0, \quad \mathbf{x} \in B, \quad \phi(\mathbf{x}) \quad \text{prescribed for } \mathbf{x} \in \partial B \quad (4)$$

where B is now the region *exterior* to the two plates. The unit normal $\mathbf{n}$ to ∂B is defined to point away from B (i.e., into a plate).

1) Regular BIE—Source Point Approaching a Plate Surface s_1^+: As $\boldsymbol{\xi} \to \mathbf{x}^+ \in \hat{s_1}^+ \in s_1^+$ (see Fig. 5), one has

$$\phi(\mathbf{x}^+) = \int_{s_1^+ - \hat{s_1}^+} \frac{\beta(\mathbf{y})}{4\pi r(\mathbf{x}^+,\mathbf{y})\epsilon} ds(\mathbf{y}) + \int_{\hat{s_1}^+} \frac{\beta(\mathbf{y})}{4\pi r(\mathbf{x}^+,\mathbf{y})\epsilon} ds(\mathbf{y}) + \int_{s_2^+} \frac{\beta(\mathbf{y})}{4\pi r(\mathbf{x}^+,\mathbf{y})\epsilon} ds(\mathbf{y}) \quad (5)$$

Here $\beta\mathbf{y} = \sigma(\mathbf{y}^+) + \sigma(\mathbf{y}^-)$, where σ is now the charge density at a point on a plate surface. The second integral is weakly singular, while the rest are usually regular. It should be noted, however, that the last integral becomes nearly weakly singular when both h and g are small.

A similar equation can be written for $\mathbf{x}^+ \in s_2^+$. For the case shown in Fig. 5, however, this is not necessary since $\beta(\mathbf{y})$ is equal and opposite on the two plates. Therefore, for this case, (5) is sufficient to solve for β on both the plates!

2) Gradient BIE—Source Point Approaching a Plate Surface s_1^+: It is first noted that for $\mathbf{x}^+ \in s_k^+ \cup s_k^-$, $k = 1, 2$

$$\sigma(\mathbf{x}) = \epsilon\frac{\partial\phi}{\partial n}(\mathbf{x}) = \epsilon\mathbf{n}(\mathbf{x}) \cdot [\nabla_{\boldsymbol{\xi}}\phi(\boldsymbol{\xi})]_{\boldsymbol{\xi}=\mathbf{x}}\,. \quad (6)$$

Consider the limit $\boldsymbol{\xi} \to \mathbf{x}^+ \in \hat{s_1}^+ \in s_1^+$. It is important to realize that this limit is meaningless for a point $\mathbf{x}$ on the edge

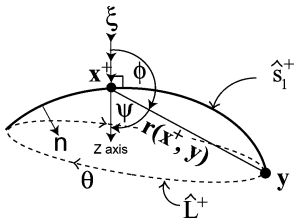

Fig. 6. Line integral for evaluation of solid angle.

of a plate, since the charge density is singular on its edges. One has

$$\sigma(\mathbf{x}^+) = \int_{s_1^+ - \hat{s_1}^+} \frac{\beta(\mathbf{y})\mathbf{r}(\mathbf{x}^+,\mathbf{y})\cdot\mathbf{n}(\mathbf{x}^+)}{4\pi r^3(\mathbf{x}^+,\mathbf{y})} ds(\mathbf{y}) + \int_{\hat{s_1}^+} \frac{\mathbf{r}(\mathbf{x}^+,\mathbf{y})\cdot[\beta(\mathbf{y})\mathbf{n}(\mathbf{x}^+) - \beta(\mathbf{x}^+)\mathbf{n}(\mathbf{y})]}{4\pi r^3(\mathbf{x}^+,\mathbf{y})} ds(\mathbf{y}) + \frac{\beta(\mathbf{x}^+)}{4\pi}\Omega\left(\hat{s_1}^+,\mathbf{x}^+\right) + \int_{s_2^+} \frac{\beta(\mathbf{y})\mathbf{r}(\mathbf{x}^+,\mathbf{y})\cdot\mathbf{n}(\mathbf{x}^+)}{4\pi r^3(\mathbf{x}^+,\mathbf{y})} ds(\mathbf{y}). \quad (7)$$

In (7), the solid angle subtended by the surface element $\hat{s_1}^+$ at the point $\mathbf{x}^+$ is (see [29]) and Fig. 6):

$$\Omega\left(\hat{s_1}^+,\mathbf{x}^+\right) = \oint_{\hat{s_1}^+} \frac{\mathbf{r}(\mathbf{x}^+,\mathbf{y})\cdot\mathbf{n}(\mathbf{y})}{r^3(\mathbf{x}^+,\mathbf{y})} ds(\mathbf{y}) = \int_0^{2\pi} [1-\cos(\psi(\theta))]\, d\theta \quad (8)$$

where the symbol $\oint$ denotes the Finite Part (FP) of the integral in the sense of Mukherjee [30], [31].

Equations (7) and (8) give the final equation

$$\frac{1}{2}\left[\sigma(\mathbf{x}^+) - \sigma(\mathbf{x}^-)\right] = \int_{s_1^+ - \hat{s_1}^+} \frac{\beta(\mathbf{y})\mathbf{r}(\mathbf{x}^+,\mathbf{y})\cdot\mathbf{n}(\mathbf{x}^+)}{4\pi r^3(\mathbf{x}^+,\mathbf{y})} ds(\mathbf{y}) + \int_{\hat{s_1}^+} \frac{\mathbf{r}(\mathbf{x}^+,\mathbf{y})\cdot[\beta(\mathbf{y})\mathbf{n}(\mathbf{x}^+) - \beta(\mathbf{x}^+)\mathbf{n}(\mathbf{y})]}{4\pi r^3(\mathbf{x}^+,\mathbf{y})} ds(\mathbf{y}) - \frac{\beta(\mathbf{x}^+)}{4\pi}\int_0^{2\pi}\cos(\psi(\theta))\, d\theta + \int_{s_2^+} \frac{\beta(\mathbf{y})\mathbf{r}(\mathbf{x}^+,\mathbf{y})\cdot\mathbf{n}(\mathbf{x}^+)}{4\pi r^3(\mathbf{x}^+,\mathbf{y})} ds(\mathbf{y}). \quad (9)$$

Here (see Fig. 6), a local coordinate system (x, y, z) is set up with the origin at $\mathbf{x}^+$ such that the positive z axis intersects the surface $\hat{s_1}^+$. Now, ψ is the angle between the positive z axis and $\mathbf{r}(\mathbf{x}^+,\mathbf{y})$ with $\mathbf{y} \in \hat{L}^+$, and θ the angle between the positive x axis and the projection of $\mathbf{r}(\mathbf{x}^+,\mathbf{y})$ in the xy plane.

In the above, the second integral on the right-hand side (RHS) is weakly singular, while the rest are usually regular. The last integral, however, becomes nearly strongly singular if both the thickness h and the gap g are small. Once β is known on both plates, (9) can be used, *as a postprocessing step*, to obtain σ^+ and σ^- on both plates.

C. Boundary Integral Equations in the Lagrangian Formulation

The Boundary Integral Equations (5) and (9), in a Lagrangian framework, are presented next.

From Nanson's law [32], one has

$$\mathbf{n}ds = J\mathbf{N}\cdot\mathbf{F}^{-1}dS \quad (10)$$

where $\mathbf{n}$ and $\mathbf{N}$ are unit normal vectors to ∂b and ∂B, at generic points $\mathbf{x}$ and $\mathbf{X}$, respectively, $\mathbf{F} = \partial\mathbf{x}/\partial\mathbf{X}$ is the deformation gradient, $J = det(\mathbf{F})$ and dS is an area element on ∂B. Here, $\mathbf{X}$ and $\mathbf{x}$ denote coordinates in the undeformed and deformed configurations, respectively.

From (10)

$$ds = J|\mathbf{N}\cdot\mathbf{F}^{-1}|dS. \quad (11)$$

Next, define Σ, the charge density per unit undeformed surface area. Since $\Sigma dS = \sigma ds$, one has

$$\Sigma = J\sigma|\mathbf{N}\cdot\mathbf{F}^{-1}|. \quad (12)$$

Also, define

$$B = \Sigma^+ + \Sigma^-. \quad (13)$$

1) Lagrangian Version of the Regular BIE: The Lagrangian version of (5) becomes

$$\phi\left(\mathbf{x}^+(\mathbf{X}^+)\right) = \int_{S_1^+ - \hat{S_1}^+} \frac{B(\mathbf{Y})dS(\mathbf{Y})}{4\pi R(\mathbf{X}^+,\mathbf{Y})\epsilon} + \int_{\hat{S_1}^+} \frac{B(\mathbf{Y})dS(\mathbf{Y})}{4\pi R(\mathbf{X}^+,\mathbf{Y})\epsilon} + \int_{S_2^+} \frac{B(\mathbf{Y})dS(\mathbf{Y})}{4\pi R(\mathbf{X}^+,\mathbf{Y})\epsilon} \quad (14)$$

where

$$\begin{aligned}\mathbf{r}\left(\mathbf{x}(\mathbf{X}),\mathbf{y}(\mathbf{Y})\right) &\equiv \mathbf{R}(\mathbf{X},\mathbf{Y}) \\ &= \mathbf{y}(\mathbf{Y}) - \mathbf{x}(\mathbf{X}) \\ &= \mathbf{Y} + \mathbf{u}(\mathbf{Y}) - \mathbf{X} - \mathbf{u}(\mathbf{X}) \quad (15)\\ r\left(\mathbf{x}(\mathbf{X}),\mathbf{y}(\mathbf{Y})\right) &\equiv R(\mathbf{X},\mathbf{Y}) \\ &= |\mathbf{R}(\mathbf{X},\mathbf{Y})| \quad (16)\end{aligned}$$

with $\mathbf{u}$ denoting the displacement at a point in B.

Also

$$\mathbf{h}(\mathbf{y}) = -\frac{\sigma^2(\mathbf{y})}{2\epsilon}\mathbf{n} \tag{17}$$

$$\int_{\partial B} \mathbf{H} dS = \int_{\partial b} \mathbf{h} ds \tag{18}$$

where $\mathbf{h}$ and $\mathbf{H}$ are the tractions per unit deformed and undeformed surface areas, respectively. Using (17), (18), (10) and (12), one gets

$$\mathbf{H} = -\frac{J\sigma^2 \mathbf{N}\cdot\mathbf{F}^{-1}}{2\epsilon} = -\frac{\Sigma^2}{2J\epsilon}\frac{\mathbf{N}\cdot\mathbf{F}^{-1}}{|\mathbf{N}\cdot\mathbf{F}^{-1}|^2}. \tag{19}$$

2) Lagrangian Version of the Gradient BIE: The Lagrangian version of (9) is derived as follows.

The first, second and third terms on the RHS of (9) are written as shown in (20)–(22) at the bottom of the page.

The fourth term is treated in the same way as the first.

One can now multiply the entire equation by $J(\mathbf{X}^+)|\mathbf{N}\cdot\mathbf{F}^{-1}|(\mathbf{X}^+)$, use the midplane values for (membrane assumption) $\mathbf{F}(\mathbf{X}^+) = \mathbf{F}(\mathbf{X}^-)$, and use the fact that $\mathbf{N}(\mathbf{X}^+) = -\mathbf{N}(\mathbf{X}^-)$. The resulting equation has the form as shown in (23) at the bottom of the page.

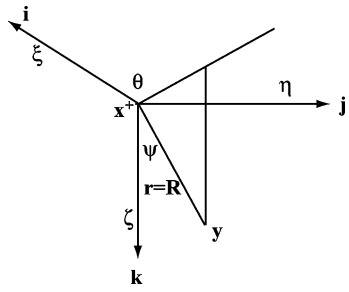

Fig. 7. Spherical polar coordinates for evaluation of the solid angle.

The integral $I = \int_0^{2\pi} \cos(\psi(\theta))d\theta$ can be evaluated from a Lagrangian approach as follows. Referring to Fig. 7, and (15), one has

$$\begin{aligned} \xi &= r\sin(\psi)\cos(\theta), \\ \eta &= r\sin(\psi)\sin(\theta), \\ \zeta &= r\cos(\psi) \end{aligned} \tag{24}$$

$$\mathbf{R}(\mathbf{X}^+, \mathbf{Y}) = \mathbf{r}(\mathbf{x}^+, \mathbf{y}) = \xi\mathbf{i} + \eta\mathbf{j} + \zeta\mathbf{k}. \tag{25}$$

Now, for any point $\mathbf{y}$ on the boundary of $\hat{s_1}^+$ (and, therefore, $\mathbf{Y}$ on the boundary of $\hat{S_1}^+$) one has

$$\mathbf{R}(\mathbf{X}^+, \mathbf{Y}) = \mathbf{Y} + \mathbf{u}(\mathbf{Y}) - \mathbf{X}^+ - \mathbf{u}(\mathbf{X}^+). \tag{26}$$

The algorithm for evaluating the integral I is described next.

$$\text{First term} = \int_{S_1^+ - \hat{S_1}^+} \frac{B(\mathbf{Y})\mathbf{R}(\mathbf{X}^+, \mathbf{Y}) \bullet J(\mathbf{X}^+)(\mathbf{N}\cdot\mathbf{F}^{-1})(\mathbf{X}^+)}{4\pi R^3(\mathbf{X}^+, \mathbf{Y}) J(\mathbf{X}^+)|\mathbf{N}\cdot\mathbf{F}^{-1}|(\mathbf{X}^+)} dS(\mathbf{Y}) \tag{20}$$

$$\text{Second term} = \int_{\hat{S_1}^+} \frac{\mathbf{R}(\mathbf{X}^+, \mathbf{Y}) \bullet \left[B(\mathbf{Y})J(\mathbf{X}^+)(\mathbf{N}\cdot\mathbf{F}^{-1})(\mathbf{X}^+) - B(\mathbf{X}^+)J(\mathbf{Y})(\mathbf{N}\cdot\mathbf{F}^{-1})(\mathbf{Y})\right]}{4\pi R^3(\mathbf{X}^+, \mathbf{Y}) J(\mathbf{X}^+)|\mathbf{N}\cdot\mathbf{F}^{-1}|(\mathbf{X}^+)} dS(\mathbf{Y}) \tag{21}$$

$$\text{Third term} = -\frac{B(\mathbf{X}^+)}{4\pi J(\mathbf{X}^+)|\mathbf{N}\cdot\mathbf{F}^{-1}|(\mathbf{X}^+)} \int_0^{2\pi} \cos\left(\psi(\theta)\right) d\theta. \tag{22}$$

$$\begin{aligned} \frac{1}{2}\left[\Sigma(\mathbf{X}^+) - \Sigma(\mathbf{X}^-)\right] = &\int_{S_1^+ - \hat{S_1}^+} \frac{B(\mathbf{Y})\mathbf{R}(\mathbf{X}^+, \mathbf{Y}) \bullet J(\mathbf{X}^+)(\mathbf{N}\cdot\mathbf{F}^{-1})(\mathbf{X}^+)}{4\pi R^3(\mathbf{X}^+, \mathbf{Y})} dS(\mathbf{y}) \\ &+ \int_{\hat{S_1}^+} \frac{\mathbf{R}(\mathbf{X}^+, \mathbf{Y}) \bullet \left[B(\mathbf{Y})J(\mathbf{X}^+)(\mathbf{N}\cdot\mathbf{F}^{-1})(\mathbf{X}^+) - B(\mathbf{X}^+)J(\mathbf{Y})(\mathbf{N}\cdot\mathbf{F}^{-1})(\mathbf{Y})\right]}{4\pi R^3(\mathbf{X}^+, \mathbf{Y})} dS(\mathbf{Y}) \\ &- \frac{B(\mathbf{X}^+)}{4\pi} \int_0^{2\pi} \cos\left(\psi(\theta)\right) d\theta + \int_{S_2^+} \frac{B(\mathbf{Y})\mathbf{R}(\mathbf{X}^+, \mathbf{Y}) \bullet J(\mathbf{X}^+)(\mathbf{N}\cdot\mathbf{F}^{-1})(\mathbf{X}^+)}{4\pi R^3(\mathbf{X}^+, \mathbf{Y})} dS(\mathbf{Y}). \end{aligned} \tag{23}$$

1) Given $X_1^+, X_2^+, X_3^+, \Theta, Y_2 = f(Y_1)$, find Y_1, Y_2, Y_3 from

$$Y_2 = f(Y_1), \quad Y_2 = \left(Y_1 - X_1^+\right)\tan(\Theta) + X_2^+, \quad Y_3 = X_3^+. \tag{27}$$

Here $Y_2 = f(Y_1)$ is the equation of the boundary of $\hat{S_1}^+$ and the angle Θ at $\mathbf{X}^+$ corresponds to θ at $\mathbf{x}^+$.

2) Find $\mathbf{R}(\mathbf{X}^+, \mathbf{Y})$ from (26).

3) Now obtain the corresponding values of the angles ψ and θ from

$$\cos(\psi) = \frac{\mathbf{R}\cdot\mathbf{k}}{R}, \quad \cos(\theta) = \frac{\mathbf{R}\cdot\mathbf{i}}{R\sin(\psi)}, \quad \sin(\theta) = \frac{\mathbf{R}\cdot\mathbf{j}}{R\sin(\psi)}. \tag{28}$$

4) Finally

$$I = \int_0^{2\pi} \cos\left(\psi(\Theta)\right)\frac{d\theta}{d\Theta}d\Theta. \tag{29}$$

The quantity $d\theta/d\Theta$ is determined as follows.

5) First, the quantities $\partial Y_k/\partial\Theta$, $k = 1, 2, 3$, are obtained from the differentiated versions of (27) with respect to Θ; i.e., from

$$\begin{aligned}\frac{\partial Y_2}{\partial\Theta} &= f'(Y_1)\frac{\partial Y_1}{\partial\Theta}\\ \frac{\partial Y_2}{\partial\Theta} &= \frac{\partial Y_1}{\partial\Theta}\tan(\Theta) + \left(Y_1 - X_1^+\right)\sec^2(\Theta)\\ \frac{\partial Y_3}{\partial\Theta} &= 0.\end{aligned} \tag{30}$$

Next, it is noted that $\partial y_i/\partial\Theta$ and $\partial x_i/\partial\Theta$ are

$$\frac{\partial y_i}{\partial\Theta} = F_{ik}(Y)\frac{\partial Y_k}{\partial\Theta}, \quad \frac{\partial x_i}{\partial\Theta} = F_{ik}(X)\frac{\partial X_k}{\partial\Theta} = 0. \tag{31}$$

Finally, differentiate

$$\tan(\theta) = \frac{y_2 - x_2^+}{y_1 - x_1^+}. \tag{32}$$

to get

$$\frac{d\theta}{d\Theta} = \frac{\left(y_1 - x_1^+\right)\frac{\partial y_2}{\partial\Theta} - \left(y_2 - x_2^+\right)\frac{\partial y_1}{\partial\Theta}}{\sec^2(\theta)\left(y_1 - x_1^+\right)^2} \tag{33}$$

3) Two Plates Close Together: For cases in which the gap $2g$ between the plates in Fig. 5 is also small, the last integral on the RHS of (5) must be treated as nearly weakly singular. In this case, this integral should be written as

$$\begin{aligned}&\int_{s_2^+} \frac{\beta(\mathbf{y})}{4\pi r(\mathbf{x}^+,\mathbf{y})\epsilon}ds(\mathbf{y})\\ &= \int_{s_2^+ - \hat{s_2}^+} \frac{\beta(\mathbf{y})}{4\pi r(\mathbf{x}^+,\mathbf{y})\epsilon}ds(\mathbf{y}) + \int_{\hat{s_2}^+} \frac{\beta(\mathbf{y}) - \beta(\tilde{\mathbf{x}}^+)}{4\pi r(\mathbf{x}^+,\mathbf{y})\epsilon}ds(\mathbf{y})\\ &\quad + \frac{\beta(\tilde{\mathbf{x}}^+)}{4\pi\epsilon}\int_{s_2^+} \frac{1}{r(\mathbf{x}^+,\mathbf{y})}ds(\mathbf{y})\end{aligned} \tag{34}$$

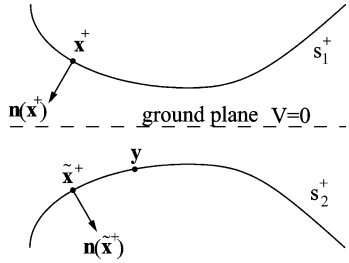

Fig. 8. Symmetric deformation of two plates.

where $\tilde{\mathbf{x}}^+ \in \hat{s_2}^+$. The first and second integrals on the RHS of (34) are regular. (The second integral is $\mathcal{O}(\tilde{r}/r)$ where $\tilde{r} = |\mathbf{y} - \tilde{\mathbf{x}}^+|$. As $\tilde{r} \to 0$, $r \to 2g + h$, so that this integrand $\to 0$.) The last integral is nearly singular. A procedure for accurate evaluation of nearly singular integrals is presented in [20] and also in Section V of the present paper.

Also, the last integral on the RHS of (9) now becomes nearly strongly singular. This integral, called J, can be evaluated as follows. One can write

$$\begin{aligned}J = &\int_{s_2^+ - \hat{s_2}^+} \frac{\beta(\mathbf{y})\mathbf{r}(\mathbf{x}^+,\mathbf{y})\cdot\mathbf{n}(\mathbf{x}^+)}{4\pi r^3(\mathbf{x}^+,\mathbf{y})}ds(\mathbf{y})\\ &+ \int_{\hat{s_2}^+} \frac{\mathbf{r}(\mathbf{x}^+,\mathbf{y})\cdot\left[\beta(\mathbf{y})\mathbf{n}(\mathbf{x}^+) - \beta(\tilde{\mathbf{x}}^+)\mathbf{n}(\mathbf{y})\right]}{4\pi r^3(\mathbf{x}^+,\mathbf{y})}ds(\mathbf{y})\\ &+ \frac{\beta(\tilde{\mathbf{x}}^+)}{4\pi}\Omega\left(\hat{s_2}^+, \mathbf{x}^+\right)\end{aligned} \tag{35}$$

where (see Fig. 6):

$$\begin{aligned}\Omega\left(\hat{s_2}^+, \mathbf{x}^+\right) &= \int_{\hat{s_2}^+} \frac{\mathbf{r}(\mathbf{x}^+,\mathbf{y})\cdot\mathbf{n}(\mathbf{y})}{r^3(\mathbf{x}^+,\mathbf{y})}ds(\mathbf{y})\\ &= \int_0^{2\pi}\left[1 - \cos\left(\psi(\theta)\right)\right]d\theta\end{aligned} \tag{36}$$

It is noted that, in this case, the point $\mathbf{x}^+$ is slightly above $\hat{s_2}^+$ and that the second term in (36) denotes a "nearly FP" integral.

The idea of regularizing (35) with $\beta(\tilde{\mathbf{x}}^+)$ has been inspired by earlier work on evaluation of nearly singular integrals [33].

Let the integrals on the RHS of (35) be called J_1, J_2, J_3. Each of the three integrals is regular. The fact that the second integral J_2 is regular can be proved as follows.

It is assumed that the two plates always remain symmetric with respect to the ground plane, even after deformation (see Fig. 8). Their equations, therefore, are of the form $x_3 = \pm f(x_1, x_2)$. One now has

$$\mathbf{n}(\mathbf{x}^+) \propto -\mathbf{k} + \mathbf{i}f_{,1} + \mathbf{j}f_{,2}, \quad \mathbf{n}(\tilde{\mathbf{x}}^+) \propto -\mathbf{k} - \mathbf{i}f_{,1} - \mathbf{j}f_{,2}. \tag{37}$$

As $\mathbf{y} \to \tilde{\mathbf{x}}^+$

$$\begin{aligned}\left[\beta(\mathbf{y})\mathbf{n}(\mathbf{x}^+) - \beta(\tilde{\mathbf{x}}^+)\mathbf{n}(\mathbf{y})\right] &\propto \mathbf{k}\left[\beta(\tilde{\mathbf{x}}^+) - \beta(\mathbf{y})\right]\\ &\quad + [\mathbf{i}a + \mathbf{j}b]\left[\beta(\tilde{\mathbf{x}}^+) + \beta(\mathbf{y})\right]\end{aligned} \tag{38}$$

where $\mathbf{i}$, $\mathbf{j}$, $\mathbf{k}$ are Cartesian unit vectors and a and b are some numbers.

As $\mathbf{y} \to \tilde{\mathbf{x}}^+$, $\mathbf{r}(\mathbf{x}^+, \mathbf{y}) \propto -\mathbf{k}$, so that the integrand of J_2 is $\mathcal{O}(\tilde{r}/r^2)$ where $\tilde{r} = |\mathbf{y} - \tilde{\mathbf{x}}^+|$. In this limit, $\tilde{r} \to 0, r \to 2g + h$, so that the integrand of $J_2 \to 0$.

The Lagrangian version of these equations are not repeated here in the interest of brevity. They are straightforward and very similar to those given in Sections II-C1 and II-C2.

III. Mechanical Problem in the Elastic Plate

Nonlinear deformation of plates, without initial in-plane forces, are discussed here. The plates are square (side $= L$), linearly elastic, and are of uniform rectangular cross section (thickness h). The boundary condition considered here is a plate with all edges clamped. Also, the edges are immovable, i.e., $u = v = 0$ on all edges of the plate. Here $u(x, y)$ and $v(x, y)$ are the in-plane and $w(x, y)$ the transverse displacement of the midplane of the plate. The force distribution (per unit area) $\mathbf{H}(x, y)$ is applied to the plate.

A. The Model

The kinematic equations adopted here are those for a von Karman plate [34], [35]

$$\begin{bmatrix} \epsilon_{xx} \\ \epsilon_{yy} \\ \gamma_{xy} \end{bmatrix} = \begin{bmatrix} u_{,x} + \frac{1}{2}(w_{,x})^2 \\ v_{,y} + \frac{1}{2}(w_{,y})^2 \\ u_{,y} + v_{,x} + w_{,x}w_{,y} \end{bmatrix}, \quad \begin{bmatrix} \kappa_{xx} \\ \kappa_{yy} \\ \kappa_{xy} \end{bmatrix} = \begin{bmatrix} -w_{,xx} \\ -w_{,yy} \\ -2w_{,xy} \end{bmatrix} \tag{39}$$

where $[\epsilon] = [\epsilon_{xx}, \epsilon_{yy}\ \gamma_{xy}]^T$ are the in-plane strains (measured at the midplane), and $[\kappa] = [\kappa_{xx}, \kappa_{yy}, \kappa_{xy}]^T$ are the curvatures and the twist.

The constitutive equations are

$$[N] = H^{(I)}[C][\epsilon], \quad [M] = H^{(O)}[C][\kappa] \tag{40}$$

where $[N] = [N_{xx}, N_{yy}, N_{xy}]^T = h[\sigma_{xx}, \sigma_{yy}, \sigma_{xy}]^T$ are the in-plane forces per unit length, σ_{ij} are the components of stress, and $[M] = [M_{xx}, M_{yy}, M_{xy}]^T$ are the bending and twisting moments. Also

$$C = \begin{bmatrix} 1 & \nu & 0 \\ \nu & 1 & 0 \\ 0 & 0 & \frac{1}{2}(1-\nu) \end{bmatrix}, \quad H^{(I)} = \frac{Eh}{1-\nu^2}, \quad H^{(O)} = \frac{Eh^3}{12(1-\nu^2)} \tag{41}$$

with ν the Poisson's ratio of the plate material.

The membrane strain energy $\mathcal{E}^{(I)}$, the bending strain energy $\mathcal{E}^{(O)}$, and the work done W are [36]

$$\mathcal{E}^{(I)} = \frac{1}{2}\int_{\Delta} [N_x\epsilon_{xx} + N_y\epsilon_{yy} + N_{xy}\gamma_{xy}]dxdy \tag{42}$$

$$\mathcal{E}^{(O)} = \frac{1}{2}\int_{\Delta} [M_x\kappa_{xx} + M_y\kappa_{yy} + M_{xy}\kappa_{xy}]dxdy \tag{43}$$

$$W = \int_{\Delta} [H_x u + H_y v + H_z w]dxdy \tag{44}$$

where Δ is the area of the plate surface.

Using (39)–(41), the energy expressions (42)–(43) can be written in terms of the plate parameters E, ν, h and the displacement derivatives. These expressions are available in [36, pp. 313 and 95], respectively.

B. FEM Model for Plates With Immovable Edges

FEM Discretization: Each plate element has four corner nodes with 6 degrees of freedom at each node. These are u, v, w, $w_{,x}$, $w_{,y}$, $w_{,xy}$. For each element, one has

$$\begin{bmatrix} u \\ v \\ w \end{bmatrix} = \begin{bmatrix} N^{(I)} & 0 \\ 0 & N^{(O)} \end{bmatrix} \begin{bmatrix} q^{(I)} \\ q^{(O)} \end{bmatrix} \tag{45}$$

with

$$\begin{aligned} \left[N^{(I)}(x,y)\right] &= \begin{bmatrix} N_1 & 0 & N_2 & 0 & N_3 & 0 & N_4 & 0 \\ 0 & N_1 & 0 & N_2 & 0 & N_3 & 0 & N_4 \end{bmatrix} \\ \left[N^{(O)}(x,y)\right] &= [P_1, P_2, \ldots, P_{16}] \end{aligned} \tag{46}$$

$$\begin{aligned} \left[q^{(I)}\right] &= [u_1, v_1, \ldots, u_4, v_4]^T \\ \left[q^{(O)}\right] &= \left[w_1, (w_{,x})_1, (w_{,y})_1, (w_{,xy})_1, \ldots, w_4, (w_{,x})_4, (w_{,y})_4, (w_{,xy})_4\right]^T. \end{aligned} \tag{47}$$

Here N_k and P_k are bilinear interpolation functions [10] and $[q^{(I)}]$ and $[q^{(O)}]$ contain the appropriate nodal degrees of freedom.

Define

$$\begin{aligned} [D] &= \begin{bmatrix} w_{,x} & 0 \\ 0 & w_{,y} \\ w_{,y} & w_{,x} \end{bmatrix} \\ [G] &= \begin{bmatrix} N^{(O)}_{,x} \\ N^{(O)}_{,y} \end{bmatrix} \end{aligned} \tag{48}$$

$$\begin{aligned} \left[B^{(I)}\right] &= \begin{bmatrix} N_{1,x} & 0 & N_{2,x} & 0 & N_{3,x} & 0 & N_{4,x} & 0 \\ 0 & N_{1,y} & 0 & N_{2,y} & 0 & N_{3,y} & 0 & N_{4,y} \\ N_{1,y} & N_{1,x} & N_{2,y} & N_{2,x} & N_{3,y} & N_{3,x} & N_{4,y} & N_{4,x} \end{bmatrix} \\ \left[B^{(O)}\right] &= -\begin{bmatrix} N^{(O)}_{,xx} \\ N^{(O)}_{,yy} \\ 2N^{(O)}_{,xy} \end{bmatrix} \end{aligned} \tag{49}$$

Substituting the interpolations (45) into (42)–(44), and minimizing the potential energy, results in the element level equations

$$\begin{bmatrix} K^{(I)} & 0 \\ 0 & K^{(O)} \end{bmatrix} \begin{bmatrix} q^{(I)} \\ q^{(O)} \end{bmatrix} + \begin{bmatrix} 0 & K^{(IO)} \\ 2K^{(IO)T} & K^{(NI)} \end{bmatrix} \begin{bmatrix} q^{(I)} \\ q^{(O)} \end{bmatrix} = [P]. \tag{50}$$

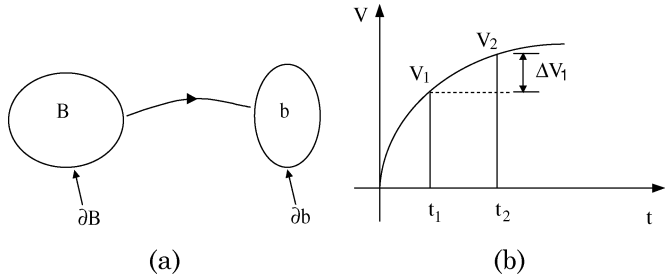

Fig. 9. (a) Deformation of body. (b) Voltage history.

The various submatrices and vector in (50) are

$$\left[K^{(I)}\right] = H^{(I)} \int\limits_{\Delta^{(e)}} \left[B^{(I)}\right]^T [C] \left[B^{(I)}\right] dxdy$$

$$\left[K^{(O)}\right] = H^{(O)} \int\limits_{\Delta^{(e)}} \left[B^{(O)}\right]^T [C] \left[B^{(O)}\right] dxdy \quad (51)$$

$$\left[K^{(IO)}\right] = \frac{H^{(I)}}{2} \int\limits_{\Delta^{(e)}} \left[B^{(I)}\right]^T [C][D][G] dxdy$$

$$\left[K^{(NI)}\right] = \frac{H^{(I)}}{2} \int\limits_{\Delta^{(e)}} ([D][G])^T [C][D][G] dxdy \quad (52)$$

$$[P] = \int\limits_{\Delta^{(e)}} \begin{bmatrix} N^{(I)} & 0 \\ 0 & N^{(O)} \end{bmatrix}^T \begin{bmatrix} \overline{H}_x \\ \overline{H}_y \\ \overline{H}_z \end{bmatrix} dxdy \quad (53)$$

where $\Delta^{(e)}$ is the area of a finite element. In (53), $[\overline{H}]$ is the resultant traction on the midsurface of the plate.

The global version of (50) is now obtained in the usual way.

Note that the in-plane and out-of-plane (bending) matrices $[K^{(I)}]$ and $[K^{(O)}]$ are $\propto h$ and h^3, respectively, the matrix $[K^{(IO)}] \propto Ah$ represents coupling between the in-plane and out-of-plane displacements, and the matrix $[K^{(NI)}] \propto A^2 h$ arises purely from the nonlinear in-plane strains.

It is well known that for the linear theory $[K^{(O)}] \ll [K^{(I)}]$ as $h \to 0$. It is very interesting, however, to note that if A/h remains $\mathcal{O}(1)$, the bending matrix $[K^{(O)}]$, which arises from the linear theory, and the matrix $[K^{(NI)}]$ from the nonlinear theory, remain of the same order as $h \to 0$. This fact has important consequences for the modeling of very thin plates [3].

IV. Schemes for Solving the Coupled Problem

A relaxation scheme and a Newton scheme to solve the coupled problem are next presented in a total Lagrangian framework.

A. Lagrangian Relaxation Scheme for the Coupled Problem

Consider, for simplicity, a thin conducting plate with a ground plane with $V = 0$. Fig. 9 shows a schematic of the applied voltage history on this plate. The deformation history $\mathbf{u}(\mathbf{x}, t)$ of this plate is obtained by a combined BEM/FEM approach as described here.

The voltage history $V(t)$ is first decomposed into a series of steps—$V_1, V_2 = V_1 + \Delta V_1, \ldots, V_{n+1} = V_n + \Delta V_n$. Consider the first step with applied voltage V_1. The BEM problem is first solved in the region exterior to the plate, and the charge density $\Sigma_1^{(0)}$ and resultant traction $\overline{\mathbf{H}}_1^{(0)}$ are obtained on the plate surface. The FEM problem with applied traction $\overline{\mathbf{H}}_1^{(0)}$ is next solved for the plate, resulting in the calculation of the displacement field $\mathbf{u}_1^{(0)}$ in the plate. The BEM problem is next solved in the region exterior to the deformed plate by the Lagrangian approach (i.e., using the undeformed plate surface). This calculation yields the next iterate of the charge density and traction, $\Sigma_1^{(1)}$ and $\overline{\mathbf{H}}_1^{(1)}$, respectively, on the plate surface. The next iterate of the displacement field in the plate, $\mathbf{u}_1^{(1)}$, is obtained next by solving the FEM problem in the plate with applied traction $\overline{\mathbf{H}}_1^{(1)}$. This iterative process is repeated until convergence. The converged values of the traction on the plate, and displacement field in the plate, at time t_1, are called $\overline{\mathbf{H}}_1$ and $\mathbf{u}_1$, respectively.

The next task is to proceed from time t_1 to t_2. To this end, the voltage increment ΔV_1 is first applied to the deformed configuration of the plate at time t_1. Solution of the corresponding BEM problem (using, again, the Lagrangian approach), yields the incremental charge density $\Delta\Sigma_1^{(0)}$ and incremental traction $\Delta\overline{\mathbf{H}}_1^{(0)}$. The displacement field $\mathbf{u}_2^{(0)}$ is obtained next by solving the FEM problem in the (undeformed) plate with the traction $\overline{\mathbf{H}}_2^{(0)} = \overline{\mathbf{H}}_1 + \Delta\overline{\mathbf{H}}_1^{(0)}$. The BEM problem is next solved with $V_2 = V_1 + \Delta V_1$. The result is the charge density $\Sigma_2^{(1)}$ and the traction $\overline{\mathbf{H}}_2^{(1)}$; followed by the FEM solution for $\mathbf{u}_2^{(1)}$. Again, this iterative process is continued until the converged values $\mathbf{u}_2$ and $\overline{\mathbf{H}}_2$ are obtained at time t_2.

The time step $t_2 - t_3$ is considered next, and so on, until the final time t_{n+1} is reached.

The algorithm employed for solving the coupled problem is outlined here.

1) Apply V_1 to B.
   Solve BEM problem on ∂B
   Get charge density $\Sigma_1^{(0)}$ and traction $\overline{\mathbf{H}}_1^{(0)}$.
2) Solve FEM problem in B with traction $\overline{\mathbf{H}}_1^{(0)}$.
   Get displacement $\mathbf{u}_1^{(0)}$ on ∂B.
3) Set $\mathrm{k} = 0$.
   Repeat.
4) Update ∂B, $\partial b_1^{(k)} = \partial B + \mathbf{u}_1^{(k)}$.
   Solve BEM problem on ∂B for $\partial b_1^{(k)}$ with V_1.
   Get charge density $\Sigma_1^{(k+1)}$ and traction $\overline{\mathbf{H}}_1^{(k+1)}$.
5) Solve FEM problem in B with traction $\overline{\mathbf{H}}_1^{(k+1)}$.
   Get displacement $\mathbf{u}_1^{(k+1)}$ on ∂B.
6) Update $\mathrm{k} = \mathrm{k} + 1$.
   Until convergence, i.e., $(|w_1^{(k+1)} - w_1^{(k)}|/|w_1^{(k)}|) \times 100 < tol$ and $(|\Sigma_1^{(k+1)} - \Sigma_1^{(k)}|/|\Sigma_1^{(k)}|) \times 100 < tol$.
   Now $t = t_1$. Get converged values $\mathbf{u}_1$, $\partial b_1 = \partial B + \mathbf{u}_1$, $\overline{\mathbf{H}}_1$.
7) Apply ΔV_1 to b_1.
   Solve BEM problem on ∂B for ∂b_1.
   Get charge density $\Delta\Sigma_1^{(0)}$, traction $\Delta\overline{\mathbf{H}}_1^{(0)}$.
8) Solve FEM problem in B with traction $\overline{\mathbf{H}}_2^{(0)} = \overline{\mathbf{H}}_1 + \Delta\overline{\mathbf{H}}_1^{(0)}$.
   Get displacement $\mathbf{u}_2^{(0)}$ on ∂B.

9) Set $\mathrm{k} = 0$.
Repeat.
10) Update ∂B, $\partial b_2^{(k)} = \partial B + \mathbf{u}_2^{(k)}$.
Solve BEM problem on ∂B for $\partial b_2^{(k)}$ with $V_2 = V_1 + \Delta V_1$.
Get charge density $\Sigma_2^{(k+1)}$ and traction $\overline{\mathbf{H}}_2^{(k+1)}$.
11) Solve FEM problem in B with traction $\overline{\mathbf{H}}_2^{(k+1)}$.
Get displacement $\mathbf{u}_2^{(k+1)}$ on ∂B.
12) Update $\mathrm{k} = \mathrm{k} + 1$.
Until convergence, i.e., $(|w_2^{(k+1)} - w_2^{(k)}|)/|w_2^{(k)}|) \times 100 < tol$ and $(|\Sigma_2^{(k+1)} - \Sigma_2^{(k)}|/|\Sigma_2^{(k)}|) \times 100 < tol$.
13) Now $t = t_2$. Get converged values $\mathbf{u}_2$, $\partial b_2 = \partial B + \mathbf{u}_2$, $\overline{\mathbf{H}}_2$.
14) Proceed until t_{n+1}.

B. Newton Scheme for Solving the Coupled Problem

The idea in this scheme is to solve the entire system of nonlinear governing equations by using the Newton method. The equations to be solved by the Newton method are the electrical domain BIE (14) and the mechanical domain FEM (50), with (23) as an auxiliary equation. The coupling (19) must also be used.

1) Residuals and Their Gradients: The appropriate residuals, as functions of $\boldsymbol{u}$ and B, as well as their gradients with respect to these variables, are given here.

The electrical residual R_E and its derivatives: The electrical residual R_E, and its derivatives with respect to B and $\mathbf{u}$ are

$$R_E(\boldsymbol{u}, B) = \phi(\mathbf{X}^+) - \int\limits_{S_1^+ - \hat{S_1}^+} \frac{B(\mathbf{Y}) dS(\mathbf{Y})}{4\pi R(\mathbf{X}^+, \mathbf{Y})\epsilon} - \int\limits_{\hat{S_1}^+} \frac{B(\mathbf{Y}) dS(\mathbf{Y})}{4\pi R(\mathbf{X}^+, \mathbf{Y})\epsilon} - \int\limits_{S_2^+} \frac{B(\mathbf{Y}) dS(\mathbf{Y})}{4\pi R(\mathbf{X}^+, \mathbf{Y})\epsilon} \tag{54}$$

$$\frac{\partial R_E}{\partial B(\mathbf{X}^+)}(\boldsymbol{u}, B) = - \int\limits_{\hat{S_1}^+} \frac{dS(\mathbf{Y})}{4\pi R(\mathbf{X}^+, \mathbf{Y})\epsilon}. \tag{55}$$

An alternative to (55) is to start from the discretized version of (54) and differentiate this equation with respect to the nodal value of B at the point $\mathbf{X}^+$.

Next, using

$$\frac{\partial}{\partial \mathbf{u}(\mathbf{X})}\left(\frac{1}{R}\right) = \frac{\mathbf{R}}{R^3}, \quad \frac{\partial}{\partial \mathbf{u}(\mathbf{Y})}\left(\frac{1}{R}\right) = -\frac{\mathbf{R}}{R^3} \tag{56}$$

one has

$$\frac{\partial R_E}{\partial \mathbf{u}(\mathbf{X}^+)}(\boldsymbol{u}, B) = - \int\limits_{S_1^+ - \hat{S_1}^+} \frac{B(\mathbf{Y})\mathbf{R}(\mathbf{X}^+, \mathbf{Y}) dS(\mathbf{Y})}{4\pi R^3(\mathbf{X}^+, \mathbf{Y})\epsilon} - \oint\limits_{\hat{S_1}^+} \frac{B(\mathbf{Y})\mathbf{R}(\mathbf{X}^+, \mathbf{Y}) dS(\mathbf{Y})}{4\pi R^3(\mathbf{X}^+, \mathbf{Y})\epsilon} - \int\limits_{S_2^+} \frac{B(\mathbf{Y})\mathbf{R}(\mathbf{X}^+, \mathbf{Y}) dS(\mathbf{Y})}{4\pi R^3(\mathbf{X}^+, \mathbf{Y})\epsilon} + B(\mathbf{X}^+) \oint\limits_{\hat{S_1}^+} \frac{\mathbf{R}(\mathbf{X}^+, \mathbf{Y}) dS(\mathbf{Y})}{4\pi R^3(\mathbf{X}^+, \mathbf{Y})\epsilon.} \tag{57}$$

The first three terms on the RHS of (57) are obtained by applying $(56)_1$ to (54), while the last one is obtained by applying $(56)_2$ and using $\partial R_E/\partial \mathbf{u}(\mathbf{Y})|_{\mathbf{Y}=\mathbf{X}^+}$. The second and fourth terms on the RHS of (57) can be combined to a single term

$$\int\limits_{\hat{S_1}^+} \frac{(B(\mathbf{X}^+) - B(\mathbf{Y}))\,\mathbf{R}(\mathbf{X}^+, \mathbf{Y}) dS(\mathbf{Y})}{4\pi R^3(\mathbf{X}^+, \mathbf{Y})\epsilon} \tag{58}$$

which is only weakly singular!

The mechanical residual $\mathbf{R}_M$ and its derivatives: The mechanical residual $\mathbf{R}_M$ is

$$\mathbf{R}_M(\boldsymbol{u}, \mathbf{B}) = \begin{bmatrix} K^{(I)} & 0 \\ 0 & K^{(O)} \end{bmatrix} \begin{bmatrix} q^{(I)} \\ q^{(O)} \end{bmatrix} + \begin{bmatrix} 0 & K^{(IO)} \\ 2K^{(IO)T} & K^{(NI)} \end{bmatrix} \begin{bmatrix} q^{(I)} \\ q^{(O)} \end{bmatrix} - [P]. \tag{59}$$

The load vector $[P]$ in (59) involves the resultant traction $\overline{\mathbf{H}}$ [see (53)]. Using (19), as well as

$$\overline{\mathbf{H}} = \mathbf{H}^+ + \mathbf{H}^-, \quad \mathbf{N} = \mathbf{N}^+ = -\mathbf{N}^-, \quad \mathbf{F} = \mathbf{F}^+ = \mathbf{F}^- \tag{60}$$

one gets

$$\overline{\mathbf{H}} = -\frac{AB}{2J\epsilon} \frac{\mathbf{N} \cdot \mathbf{F}^{-1}}{|\mathbf{N} \cdot \mathbf{F}^{-1}|^2} \tag{61}$$

where $A = \Sigma^+ - \Sigma^-$.

It is very easy to evaluate $\partial \mathbf{R}_M/\partial B = -\partial[P]/\partial B$.

The gradient $\partial \mathbf{R}_M/\partial \mathbf{u}$ has two parts. The first part comes from the first two terms on the RHS of (59). (Note from (47) that $[q^{(I)}]$ and $[q^{(O)}]$ involve the displacement components u_k, as well as the slopes, $w_{,x}$, $w_{,y}$ and twist $w_{,xy}$; and the stiffness matrices $K^{(IO)}$ and $K^{(NI)}$ [see (52), (48)] involve slopes.) For the Newton scheme employed in this work, the displacement components $[u_k] = [u, v, w]$ of $\mathbf{u}$ are independent. One, therefore, needs to evaluate derivatives such as $\partial w_{,x_m}/\partial w$, $m = 1$, 2 as well as similar derivatives for the twist $w_{,xy}$. These derivatives, as well as those required for the components of the deformation gradient $\mathbf{F}$ (see (74)), are discussed next.

The second part comes from $\partial \overline{\mathbf{H}}/\partial \mathbf{u}$ and this requires evaluation of $\partial \mathbf{F}/\partial \mathbf{u}$ and $\partial J/\partial \mathbf{u}$, together with application of the chain rule. For these calculations, it is useful, in general, to use

$$\frac{\partial F_{ij}}{\partial u_k} = \frac{\partial F_{ij}}{\partial X_m} F^{-1}_{mk}$$
$$\frac{\partial J}{\partial u_k} = J \frac{\partial F_{ij}}{\partial u_k} F^{-1}_{ji}$$
$$\frac{\partial \mathbf{F}^{-1}}{\partial \mathbf{u}} = -\mathbf{F}^{-1} \cdot \frac{\partial \mathbf{F}}{\partial \mathbf{u}} \cdot \mathbf{F}^{-1}. \tag{62}$$

Please note that derivatives of the components of $\mathbf{F}$ in this work (see (74)) are discussed below.

Finally, the auxiliary equation (23) (the gradient BIE) is viewed as

$$(1/2)A = f(\mathbf{u}, B) \tag{63}$$

and is used within each Newton iteration.

Derivatives of Displacement Gradients: First consider, for example, $\partial w_{,x}/\partial w$. One first writes $w_{,x}(x,y)$. This can be interpreted in two ways [37]

1) $w_{,x}(x, y(w,x))$; where $w_{,x}$, y are dependent variables and w, x are independent variables. Now

$$\left.\frac{\partial w_{,x}}{\partial w}\right|_x = \frac{\partial w_{,x}}{\partial y}\frac{\partial y}{\partial w} = \frac{w_{,xy}}{w_{,y}}. \tag{64}$$

2) $w_{,x}(x(w,y),y)$; where $w_{,x}$, x are dependent variables and w, y are independent variables. This time

$$\left.\frac{\partial w_{,x}}{\partial w}\right|_y = \frac{\partial w_{,x}}{\partial x}\frac{\partial x}{\partial w} = \frac{w_{,xx}}{w_{,x}}. \tag{65}$$

The average value is chosen in this work. Thus:

$$\frac{\partial w_{,x}}{\partial w} = \frac{1}{2}\left(\frac{w_{,xy}}{w_{,y}} + \frac{w_{,xx}}{w_{,x}}\right), \quad \frac{\partial w_{,y}}{\partial w} = \frac{1}{2}\left(\frac{w_{,yy}}{w_{,y}} + \frac{w_{,xy}}{w_{,x}}\right). \tag{66}$$

The derivative of the twist $w_{,xy}$ with respect to w is evaluated in similar fashion.

The derivatives of the components of $\mathbf{F}$ in (74) are derived somewhat differently. First consider the derivatives of $u_{,x}$ and $u_{,y}$ with respect to u. Start with $u_{,x}(x,y) = u_{,x}(x(u,v), y(u,v))$; and similarly for $u_{,y}$. Using the chain rule:

$$\frac{\partial}{\partial u}(u_{,x}) = u_{,xx}x_{,u} + u_{,xy}y_{,u}, \quad \frac{\partial}{\partial u}(u_{,y}) = u_{,xy}x_{,u} + u_{,yy}y_{,u}. \tag{67}$$

Similar equations are obtained for the derivatives of $v_{,x}$ and $v_{,y}$ with respect to v by replacing u with v in (67). Finally:

$$\begin{bmatrix} x_{,u} & x_{,v} \\ y_{,u} & y_{,v} \end{bmatrix} = \begin{bmatrix} u_{,x} & u_{,y} \\ v_{,x} & v_{,y} \end{bmatrix}^{-1}. \tag{68}$$

Any singularities, [e.g.,$w_{,x} = 0$ in (66)], must be handled carefully. An average value of such a quantity, from neighboring nodes, is used in this paper.

2) The Newton Algorithm: First, define

$$\mathbf{R}(\mathbf{u}, B) = \begin{bmatrix} R_E(\mathbf{u}, B) \\ \mathbf{R}_M(\mathbf{u}, B) \end{bmatrix}. \tag{69}$$

One has the Newton iterative scheme

$$\begin{bmatrix} \frac{\partial \mathbf{R}}{\partial \mathbf{u}} & \frac{\partial \mathbf{R}}{\partial B} \end{bmatrix}_n \begin{bmatrix} \Delta \mathbf{u} \\ \Delta B \end{bmatrix}_n = -\mathbf{R}_n, \tag{70}$$

$$\mathbf{u}_{n+1} = \mathbf{u}_n + \Delta \mathbf{u}_n, \quad B_{n+1} = B_n + \Delta B_n. \tag{71}$$

Starting with $n = 0$, (70) is iterated until convergence. At convergence, $\mathbf{R}_n \equiv \mathbf{R}(\mathbf{u}_n, B_n) \to 0$.

The voltage is applied in steps. The algorithm for a typical step V for the coupled scheme is described next.

1) Solve BEM on ∂B for applied voltage V.

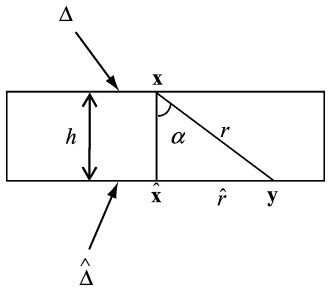

Fig. 10. Singular integrals.

2) Solve for $B^{(0)}$, substitute $B^{(0)}$ in (63) and solve for $A^{(0)}$. Use $B^{(0)}$ and $A^{(0)}$ in (61) to evaluate $\overline{\mathbf{H}}^{(0)}$.

3) Solve FEM problem in B with traction $\overline{\mathbf{H}}^{(0)}$, find displacement $\mathbf{u}^{(0)}$ on ∂B.

4) Set $k = 0$.

5) Do

6) Use (55) and (57) to solve for $\partial R_E/\partial B$ and $\partial R_E/\partial \mathbf{u}$, where $B = B^{(k)}$.

7) Next find $\partial \mathbf{R}_M/\partial B$ and $\partial \mathbf{R}_M/\partial \mathbf{u}$.

8) Use the computed values to evaluate $\mathbf{R}_k$ in (69).

9) Use $\mathbf{R}_k$ in (70) to solve for $\Delta \mathbf{u}^{(k)}$ and $\Delta B^{(k)}$.

10) Update $\mathbf{u}^{(k+1)} = \mathbf{u}^{(k)} + \Delta \mathbf{u}^{(k)}$.

11) Update $B^{(k+1)} = B^{(k)} + \Delta B^{(k)}$.

12) Update $k = k + 1$

13) Compute $displacement\ residual = (|w^{(k+1)} - w^k|/|w^k|) \times 100$.

14) While (displacement residual is high)

15) $\mathbf{u} = \mathbf{u}^{(k+1)}$

16) $\Sigma = \Sigma^{(k+1)}$

V. Numerical Implementation

A. Boundary Integral Equations for Two Plates Very Close Together

As aforementioned, the last integral on the RHS of (34) is nearly weakly singular. Similar integrals arise when a 3-D region outside a thin plate is analyzed *by the conventional BEM*. A procedure for accurate evaluation of such integrals is outlined next.

Proposed Method for the Accurate Evaluation of Nearly Weakly Singular Integrals: Consider a source point $\mathbf{x}$ on the top face of a plate and its image point $\hat{\mathbf{x}}$ on the bottom face in Fig. 10. Two kinds of singular $(\mathcal{O}(1/r))$ integrals arise—a weakly singular integral on the boundary element Δ on the top face of the plate that contains $\mathbf{x}$, and, since h is small, a nearly weakly singular integral on the boundary element $\hat{\Delta}$ (the image of Δ) on the bottom face of the plate that contains $\hat{\mathbf{x}}$ [20]. The

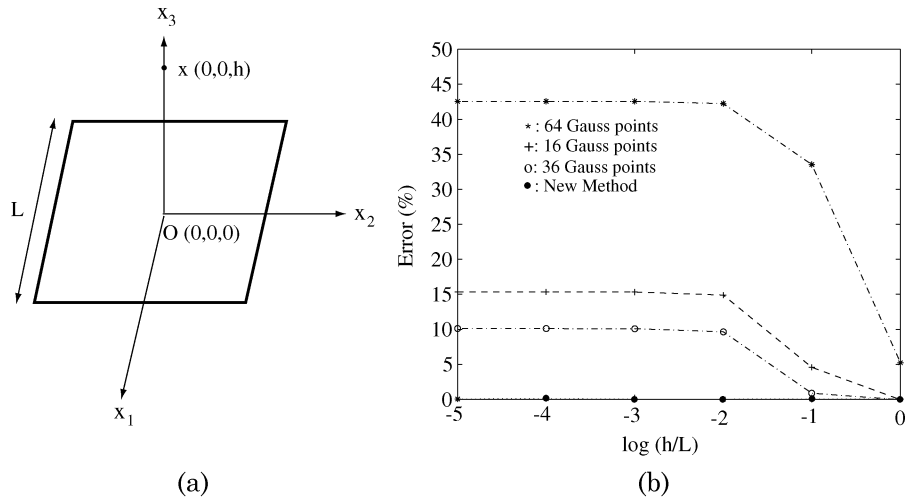

Fig. 11. (a) Numerical integration over a square element. (b) Errors in numerical integration over a square.

weakly singular integral is evaluated by employing the mapping method outlined in [38], [39]. This method transforms such integrals over rectangular (curved or flat) domains into regular 2-D triangles (4 triangles). Integrals over curved quadratic or flat linear triangles are further reduced to regular line integrals that can be easily evaluated to desired accuracy by standard Gaussian quadrature.

A simple method [20] is presented for the accurate and efficient evaluation of nearly weakly singular integrals. This approach transforms a nearly weakly singular integral into a weakly singular one; which is then evaluated by the method described in [38], [39]. A nearly weakly singular integral of interest here has the form

$$I(\mathbf{x}) = \int_{\hat{\Delta}} \frac{ds(\mathbf{y})}{r(\mathbf{x},\mathbf{y})}. \tag{72}$$

The integrand (72) is multiplied by $\hat{r}/\hat{r}$ with the result

$$I(\mathbf{x}) = \int_{\hat{\Delta}} \frac{[(\hat{r}/r)]\, ds(\mathbf{y})}{\hat{r}(\hat{\mathbf{x}},\mathbf{y})}. \tag{73}$$

Since $\hat{r}/r$ is $\mathcal{O}(1)$ and $\rightarrow 0$ as $\mathbf{y} \rightarrow \hat{\mathbf{x}}$ (i.e., as $\hat{r} \rightarrow 0$), the integrand in (73) is weakly singular, of $\mathcal{O}(1/\hat{r})$ as $\hat{r} \rightarrow 0$. Therefore, the integral (73) can be evaluated by employing the methods described in [38] and [39].

Performance of New Method: The performance of the new method is compared with that of standard Gauss integration.

Fig. 11(a) shows the source point $\mathbf{x}(0,0,h)$ and region of integration $\hat{\Delta}$ (a square of side L). Numerical results appear in Fig. 11(b). It is seen that for $h/L < 1/100$, standard Gauss integration, even with 36 Gauss points, cannot reduce the error below around 10%. By increasing the number of Gauss points to 64, the errors dramatically increases to 42%. This is due to numerical instabilities. The new method is seen to take care of these nearly weakly singular integrals very well, even for very small values of h/L.

B. Nonlinear Finite Element Analysis

It is important to point out that (50) is nonlinear due to the fact that the matrices $[K^{(IO)}]$ and $[K^{(NI)}]$ contain the gradient of w [see (48), (52)]. Newton iterations are used to solve (50) once the transverse displacement w becomes significant.

C. BEM/FEM Coupling

Both the relaxation scheme and Newton schemes are used for the coupling of BEM and FEM solutions. In the relaxation scheme, the BEM problem is solved for charge densities. Tractions are obtained and the resultant tractions are transferred to the FEM domain to obtain the deformed configuration. The FEM solves for the displacements and displacement gradients on a thin plate midsurface and returns them back to the BEM. The BEM problem is solved again for the deformed configuration, and new charge densities are obtained. This process is implemented iteratively until convergence. The deformation gradient is obtained with a membrane assumption as shown next

$$F = \begin{bmatrix} 1+u_{,x} & u_{,y} & 0 \\ v_{,x} & 1+v_{,y} & 0 \\ w_{,x} & w_{,y} & 1 \end{bmatrix}. \tag{74}$$

Here, u, v and w represent the nodal displacements. For the Newton scheme, the nonlinear equations are solved together using Newton iterations. This procedure has been described before in Section IV-B.

D. Discretization

The BEM models only the top surface (s_k^+, see Fig. 5) and the FEM the midsurface of each plate. No distinction need to be made between the top and mid surfaces since the plates are very thin. The mesh used here is as follows. The BEM and FEM domains each use 64 Q4 elements. Of course, the BEM has one degree of freedom per node and the FEM has 6 degrees of freedom at each node.

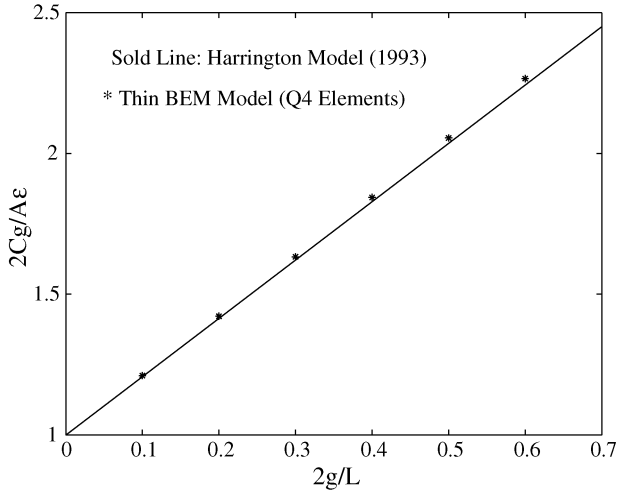

Fig. 12. Capacitance check of BEM model.

VI. Numerical Results

A. Code Verification

The computer code with the thin BEM Lagrangian formulation has been carefully verified at several stages. Details are given here.

1) BEM for Region Exterior to a Thin Flat Plate:

Total charge: Results from the thin BEM formulation have been compared to those from Harrington's [19] model (Fig. 12). For this verification, the gap ratio $(2g/L)$ has been varied from 0.1 to 0.6 in steps of 0.1, and the resulting capacitance of the MEMS plates has been compared to the values predicted by Harrington's model. The thickness ratio h/L for this problem is chosen to be 10^{-3}, $L = 2$ mm, $A = L^2$ and $C = Q/2V$, where Q is the total charge on the top plate and V and $-V$ are the potentials on the upper and lower plates, respectively. As is evident, results form the two models agree very well. It is noted here that the two models are very similar except that Harrington used constant boundary elements.

An empirical formula for the capacitance, based on Fig. 12, can be written as

$$C = \frac{\epsilon L^2}{\gamma} + \epsilon\alpha L \tag{75}$$

where $\gamma = 2g$ is the total gap between the plates and α is the slope of the curve in Fig. 12. The dimensionless factor $\alpha \approx 2$.

Charge separation: For the two plate capacitor shown in Fig. 5, the charge on the upper plate, neglecting the effects of the fringing fields, can be written as

$$\sigma \approx \frac{\epsilon\Delta}{\gamma} \tag{76}$$

where Δ is the potential difference between the plates. With $\Delta = 2$ volts and $\gamma = 0.2L$, (76) gives $\sigma \approx 10\epsilon/L$. In [20, Table 3] (a thin plate BEM formulation), with $L = 1$, $\epsilon = 1$, has $\sigma^- = 9.907$ (at the center of the top plate with the finest mesh). (The same numerical result is obtained with the code developed for the present paper.)

Force for small voltage: From Senturia [42]

$$F = -\frac{\partial}{\partial\gamma}\left[\frac{C\Delta^2}{2}\right] = -\frac{1}{2}\frac{\partial C}{\partial\gamma}\Delta^2 \tag{77}$$

where F is the force between the plates in a two-plate capacitor.

From (75) and (77), one gets the traction magnitude H as

$$H = \frac{F}{L^2} = \frac{\Delta^2\epsilon}{2\gamma^2}. \tag{78}$$

For the case in [20, Table 3] (with $\Delta = 2$, $\gamma = 0.2L$), one has $H = 50\epsilon/L^2$.

It is noted that the traction, for small voltages, is linear in Δ^2. For larger voltages, one must use $\gamma(\mathbf{x}) = \gamma_0 - w(\mathbf{x})$ [42] (with γ_0 the initial constant gap between the plates) and H becomes a function of w.

Now (17) is used to determine the traction. Using the values of $\sigma^- = 9.907$ and $\sigma^+ = 1.47$ from [20, Table 3], one gets

$$\overline{H} = H^- - H^+ = 47.99\epsilon/L^2 \tag{79}$$

with $\overline{H}$ acting downwards on the top plate. The difference between the two results is 4%.

2) Lagrangian BEM for Region Exterior to a Curved Plate:

"Fat" plate: The proposed Lagrangian BEM algorithm has been verified before. In [24, Sec. 5.3], for example, considers a (3-D) bent cantilever beam with dimensions $20 \times 1 \times 1$. The standard (not thin plate) BEM is used here. The differences between the numerical results from an Eulerian and a Lagrangian BEM formulation are shown to be of the order of 0.1% at various points on the surface of the bent beam. The maximum difference is only 0.09% when each conductor is discretized with 738 constant boundary elements.

Thin plate/beam: A new example is presented here.

The geometry of the problem, a curved beam, is shown in Fig. 13(a). The length of the curved beam (top or bottom surface) is 1000 μm, its thickness is 10 μm, the deflection of the center of the bottom surface is 30 μm and the gap between the center of its bottom surface and the ground plane is 60 μm.

The charge distribution σ^- on the bottom surface of the beam, with $V = 1$, $\epsilon = 1$, is shown in Fig. 13(b). The solid line is the result from a standard 2-D BEM code. The $*$ symbols depict the results from the (Lagrangian) 3-D thin plate BEM code for a plate with dimensions $4000 \times 1000 \times 10$ μm. For this case, σ^- is shown along a line through the center of the lower surface of the plate, parallel to its shorter edge. The results are seen to agree quite well. Of course, perfect agreement between the two models is not expected (see [20, Tables 1 and 2]).

It should be stated here that the computer programs used to generate the results shown in Fig. 13(b) use a length scale of mm (i.e., $L = 1$ mm, $g = .06$ mm, etc.) with $\epsilon = 1$ F/mm. Therefore, the output σ^- is in $\mathrm{C}/(\mathrm{mm})^2$.

Finally, it is noted that for a straight beam [in Fig. 13(a)] with $g = .06$ mm, (76) in the form $\sigma = \epsilon\Delta/g$ yields a uniform

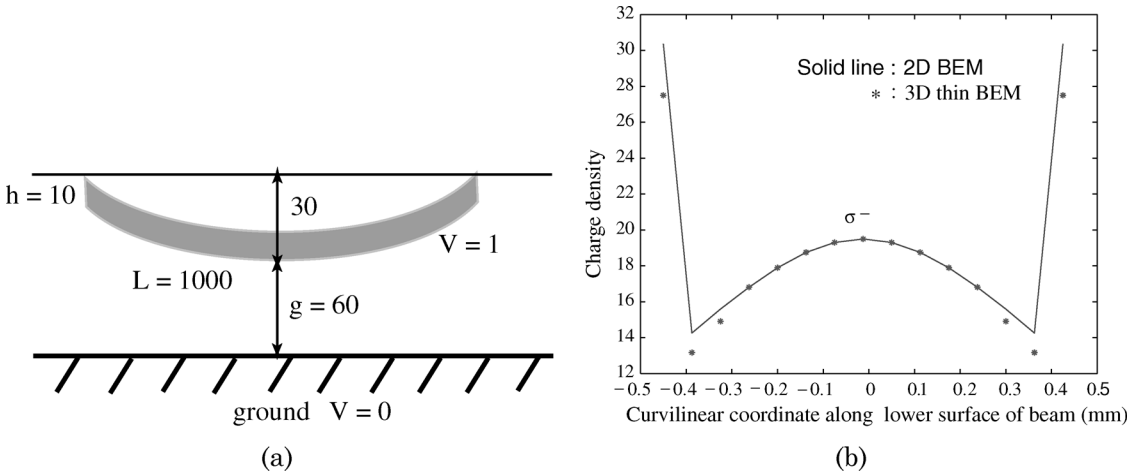

Fig. 13. (a) Schematic of curved beam with lengths in μm. (b) charge distribution σ^- along the low surface of the curved beam.

$\sigma = 1/.06 = 16.67\ \mathrm{C/(mm)^2}$. Clearly, this result is not satisfactory and a detailed calculation is needed to obtain the correct variation of charge density on a curved beam, as shown in Fig. 13(b).

3) FEM for Deformation of a Thin von Karman Plate: The FEM formulation for deformation of von Karman plates, presented in Section III of this paper, has been carefully verified earlier in [3]. The usual checks (e.g., bending deformation of a clamped square plate under uniform applied pressure) have been successfully carried out for the current rendition of the FEM code.

4) Coupling of BEM and FEM: This coupling has been carried out with two different approaches: the relaxation scheme and the Newton scheme. As seen in Section VI-B, results from these two formulations show excellent agreement. In addition, results shown in Fig. 15(b) have been compared with those from earlier work [27]. This matter is discussed in Section VI-B.

B. MEMS Plates

Material Properties: Material properties used for Silicon conductors are [40], [41]

$$E = 169\ \mathrm{GPa}, \quad \nu = 0.22, \quad \epsilon = 8.85 \times 10^{-7}\ \mathrm{F/m}. \quad (80)$$

It is assumed that the anisotropy is negligible and the plate is made up of poly-silicon material for this system.

The Problem: Deformation of a silicon MEMS plate (the silicon is doped so that it is a conductor), subjected to a progressively increasing electrostatic field, is simulated here by the coupled BEM/FEM. Each plate is clamped around its edges and two plates are used in order to have a zero voltage ground plane (the plane of symmetry) midway between them (see Fig. 14).

Two problems of interest have been studied in this analysis. For the first problem, each plate is square of side $L = 2$ mm, thickness $h = 6$ μm, and the gap g (distance between ground and the nearest plate surface) is 36 μm. Both plates are allowed to deform. The next problem studies the effect of gap on the deformation response of the MEMS plates. For this problem, the plates have a side of $L = 2$ mm and thickness $h = 2$ μm.

Results: Fig. 15(a) shows the normalized central deflection of the top plate as a function of the square of the applied voltage,

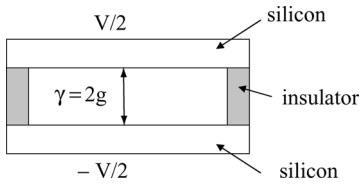

Fig. 14. Model problem for microjet.

for relatively small values of the applied voltage. This curve is linear as expected [see (78)] since H linear in V^2 gives w_0 linear in V^2.

A comparison of relaxation scheme and Newton scheme is done next. The normalized plate center deflection with applied voltage is shown in Fig. 15(b). For the relaxation scheme, the voltage is applied in a series of 0.2 V steps (max 2.4 V). This time, the initial part is linear, but the response becomes nonlinear for larger values of V (see [16, Fig. 8]). There are two reasons for this nonlinear response. The first is that the electrical force is nonlinear since $g(\mathbf{x}) = g_0 - w(\mathbf{x})$ in (78); and the impact of w becomes more and more pronounced as its value becomes larger and larger. The second is that the elastic response of the plate becomes nonlinear as w becomes larger (see Section III). This effect is often referred to as membrane stiffening. As can be seen, for an applied voltage of 1.5 V the deflection of the plate center is of the order of its thickness.

It is noted that the results from the relaxation scheme agree with those from the Newton scheme (within plotting accuracy) in Fig. 15.

A similar problem has been solved before [27] in which the Lagrangian formulation was applied but the standard (not thin plate) BEM was used. Hence, the gradient BIE (9) and its Lagrangian counterpart (23) are absent in [27]. Also, the relaxation scheme was used in that paper to couple the BEM with the FEM. Fig. 8 in [27] presents the nondimensional central deflection $\hat{w} = w_0/h$ as a function of nondimensionalized voltage

$$\hat{V}^2 = \frac{\epsilon L^5 V^2}{2\gamma^3 EI} \quad (81)$$

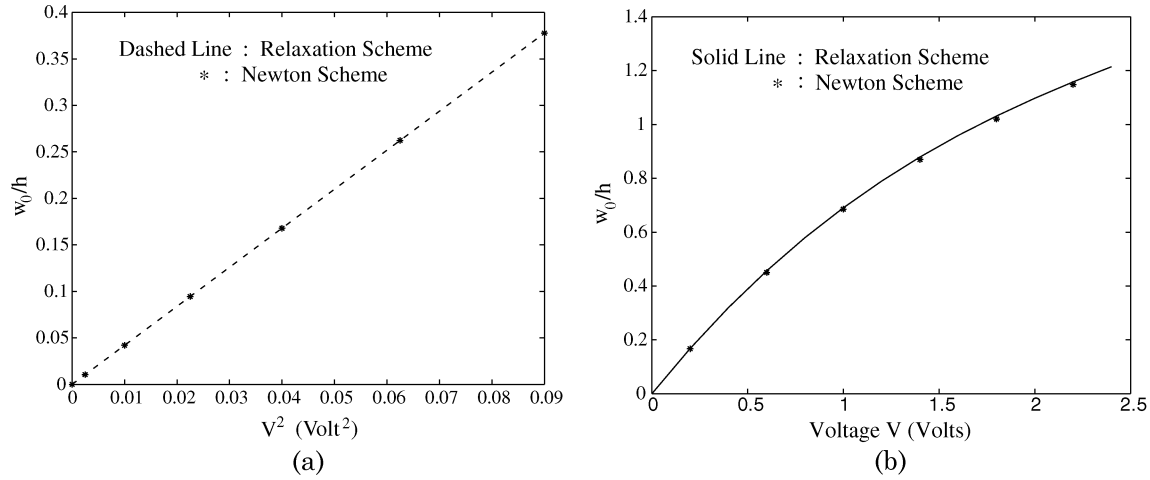

Fig. 15. Response behavior of microjet device. (a) For low voltages. (b) For higher voltages. $L = 2$ mm, $h = 6\ \mu$m, $g = 36\ \mu$m.

TABLE I
COMPARISON OF RESULTS FROM THE PRESENT COMPUTER CODE WITH THOSE FROM [27]. $L = 3$ mm, $h = 0.03$ mm, $\gamma = 1$ mm

$\hat{V}^2 \times 10^6$	$\hat{w}$ (present)	$\hat{w}$ [27]
2	1.46	1.44
4	1.948	1.92
6	2.246	2.35
8	2.451	2.44

where the moment of inertia of the plate cross section $I = Lh^3/12$. The two-plate configuration shown in Fig. 14 was also used in [27] with the following values of geometrical parameters: $L = 3$ mm, $h/L = 0.01$ and $\gamma = 1$ mm; the physical parameters being those given in (80). A comparison of results from [27, Fig. 8] and those from the computer code developed in the present paper, appear in Table I. The results are seen to agree quite well. An L_2 norm of the difference between the two results is defined as

$$\epsilon = \frac{\left[\sum_{i=1}^{N}\left(\hat{w}_i^{(1)} - \hat{w}_i^{(2)}\right)^2\right]^{1/2}}{\sqrt{N}\left|\hat{w}_{\max}^{(1)}\right|} \times 100. \qquad (82)$$

where N is the number of points, $\hat{w}^{(1)}$ denotes the present results and $\hat{w}^{(2)}$ those from [27]. From the results in Table I, one gets $\epsilon = 2.246\%$.

The effect of the initial gap between the MEMS plates is shown in Fig. 16. These results are obtained from the Newton scheme. It can be seen that when the plates are moderately densely packed, even a few millivolts of applied voltage induces large deformations in the conducting plate. It is also observed that the deformations are highly nonlinear when the voltage is high. The results for the smallest initial gap $(5h)$ are considered to be reliable up to about 60 mV. Beyond that, the gap (between the center of the plate and the ground plane) is $O(h)$ and the numerical results start becoming unreliable—each iteration takes a long time to converge. It is conjectured that the plate, at this stage, is experiencing the onset of pull-in, but this requires further investigation. The issue of very densely packed plates is discussed in Section VII.

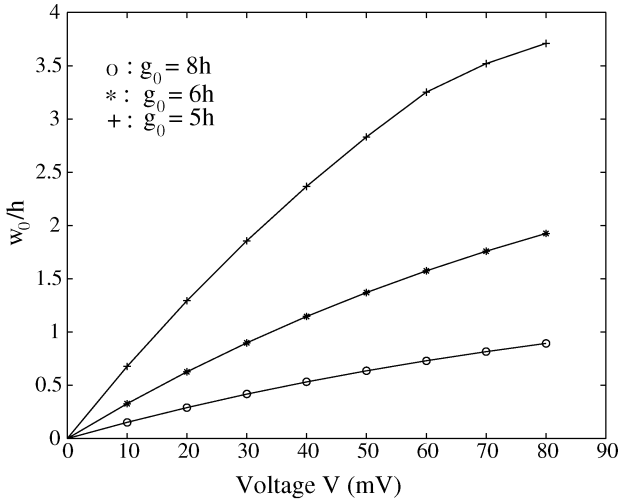

Fig. 16. Effect initial gap on MEMS response behavior. $L = 2$ mm, $h = 2\ \mu$m.

It is interesting to comment on the competing nonlinearities in Figs. 15 and 16. As stated earlier in this section, the electrical nonlinearity arises from the reducing gap $g(\mathbf{x}) = g_0 - w(\mathbf{x})$ due to plate deformation. This causes progressive increase of the electrostatic force between the plates, leading to larger deformation at a given voltage (compared to the case $g = g_0$)—a softening effect. The mechanical nonlinearity, on the other hand, has a stiffening effect.

The gap g at the plate center only reduces from 36 μm to around 29 μm at around 2 V in Fig. 15(b). The nonlinearity exhibited in this figure, therefore, is primarily mechanical in origin. The same is largely true for the cases $g_0 = 8h = 16\ \mu$m and $g_0 = 6h = 12\ \mu$m in Fig. 16. Here the gap at the plate center reduces to, approximately, 14.5 μm and 8.5 μm, respectively, at 80 mV (a reduction of $\approx$10% and 30%), so that the nonlinearity is still largely mechanical (although the electrical effect is starting to kick-in for $g_0 = 6h$).

The situation, however, is quite different for the case $g_0 = 5h$ in Fig. 16. In this case, the gap at the plate center reduces from 10 μm to around 4 μm at 56 mV (a 60% reduction), so that the softening due to the electrical nonlinearity plays an important role. It is seen in Fig. 16, however, that the membrane effect does dominate the electrical effect, so that the resulting curve has decreasing slope. In fact, the plate is close to pull-in at around 60 mV. A short discussion of pull-in is presented in Section VII.

VII. Discussion

This paper presents a first attempt at a fully Lagrangian approach for the analysis of coupled 3-D MEMS systems made up of thin structural elements that are relatively closely packed. The Lagrangian approach uses only the undeformed configuration (usually simple) of a plate for both the electrical and mechanical analyses—thus obviating the need to discretize any deformed configuration.

The hybrid BEM/FEM approach is able to handle thin plates (with $h/L = 1/1000$) efficiently. Convergence is achieved for relatively large voltage steps with only a few iterations. The proposed simple new approach for accurate evaluation of nearly weakly singular integrals works well. (It is noted that although the idea is illustrated in Section V-A for flat plates, it is also successfully employed when the plates become curved due to deformation.) It is seen from Fig. 15(b) that the nonlinear effects can be very significant. Therefore, the nonlinear FEM model, employed in this work, is of crucial importance.

An important practical matter in MEMS is the pull-in voltage. Stable equilibrium of a deformed plate demands that the applied electrical force on it must be in stable equilibrium with the restoring elastic (spring) force. A well-known calculation considers the simpler problem of a *rigid spring loaded plate subjected to increasing voltage* V that is attracted towards a fixed parallel plate (ground) at zero voltage, with g_0 the initial gap between the plate and the ground [42]. The moving plate always moves down parallel to its original position. It is proved in [42] that stable equilibrium is lost and pull-in occurs when the current gap, that decreases with increasing V, reaches

$$g_{PI} = (2/3)g_0. \tag{83}$$

The problem considered in this paper is that of a deformable plate that is clamped on all its edges. It is seen in Fig. 16 that, with $g_0 = 5h$, the gap at the center of the plate $\approx 2h$ at $V \approx 56$ mV, i.e., $\approx (2/5)g_0$. This does not contradict (83) since the plate in the present work is deformable and the gap between its clamped edges and the ground, for example, always remains g_0; while g between the moving rigid plate in [42] and the ground progressively decreases but always remains uniform. Also, the stiffness k in the rigid plate problem remains constant while it increases in the deformable plate problem due to membrane stiffening. An electrostatic deformation analysis of a (deformable) clamped-clamped beam [43] obtained the deflection at pull-in to be $\approx .57g_0$ which compares favorably with the present result of the plate approaching pull-in at a central deflection of around $0.6g_0$. Further investigation of the pull-in phenomenon for deformable plates is planned for the future.

The next planned research task is 3-D dynamic analysis of the problem considered in this paper. Dynamic MEMS analysis with a fully Lagrangian approach is expected to provide many additional benefits relative to the traditional approach that uses Lagrangian mechanical but Eulerian electrical analysis (see [26] where the 2-D dynamic problem has been studied recently). Eventually, the motion of the fluid between the plates must be modelled in the problem discussed in [2]. This motion would cause the voltages to be increased substantially, especially at higher frequencies, due to the damping and compressibility effects of the fluid between the plates. A preliminary BEM analysis of Stoke's flow around slowly moving rigid thin plates appears in [28].

Successful modelling of MEM structures with plates that are packed very densely together (e.g., with gaps that are of the order of a plate thickness) is still an open problem. One possible idea for solving this problem is to extrapolate BEM solutions for traction distributions as a function of gap size for $g \geq 10h$, down to gaps $\approx O(\mathrm{h})$. For electrostatic problems of interest in this work here, this extrapolation should be guided by (78), noting that the impact of w on $\overline{\mathbf{H}}$ quickly becomes significant when deformation of a plate starts with small γ_0. This problem is a topic of continuing research.

References

[1] A. Frangi and A. Digioia, "Multipole BEM for the evaluation of damping forces on MEMS," *Comput. Mech.*, vol. 37, pp. 24–31, 2005.

[2] M. Roman and N. Aubry, "Design and fabrication of electrostatically actuated synthetic microjets," in *ASME Paper No. IMECE2003-41579*. New York: Amer. Soc. Mechan. Eng., 2003.

[3] Z. Bao, S. Mukherjee, M. Roman, and N. Aubry, "Nonlinear vibrations of beams strings plates and membranes without initial tension," *ASME J. Appl. Mech.*, vol. 71, pp. 551–559, 2004.

[4] S. C. Ko, Y. C. Kim, S. S. Lee, S. H. Choi, and S. R. Kim, "Micromachined piezoelectric membrane acoustic device," *Sens. Actuators A, Phys.*, vol. 103, pp. 130–134, 2003.

[5] S. Mukherjee, *Boundary Element Methods in Creep and Fracture*. London, U.K.: Applied Science, 1982.

[6] P. K. Banerjee, *The Boundary Element Methods in Engineering*. Maidenhead, Berkshire, U.K.: McGraw-Hill Europe, 1994.

[7] A. Chandra and S. Mukherjee, *Boundary Element Methods in Manufacturing*. New York: Oxford Univ. Press, 1997.

[8] M. Bonnet, *Boundary Integral Equation Methods for Solids and Fluids*. New York: Wiley, 1999.

[9] S. Mukherjee and Y. X. Mukherjee, *Boundary Methods: Elements, Contours and Nodes*. Boca Raton, FL: CRC, 2005.

[10] T. Y. Yang, *Finite Element Structural Analysis*. Englewood Cliffs, NJ: Prentice-Hall, 1986.

[11] O. C. Zienkiewicz and R. L. Taylor, *The Finite Element Method*, 4th ed. Berkshire, U.K.: McGraw-Hill, 1994, vol. 1,2.

[12] T. J. R. Hughes, *The Finite Element Method: Linear Static and Dynamic Finite Element Analysis*. Mineola, NY: Dover, 2000.

[13] S. D. Senturia, R. M. Harris, B. P. Johnson, S. Kim, K. Nabors, M. A. Shulman, and J. K. White, "A computer-aided design system for microelectromechanical systems (MEMCAD)," *J. Microelectromech. Syst.*, vol. 1, pp. 3–13, 1992.

[14] K. Nabors and J. White, "FastCap: a multi-pole accelerated 3-D capacitance extraction program," *IEEE Trans. Comput.-Aided Des. Integr. Circuits Syst.*, vol. 10, pp. 1447–1459, 1991.

[15] J. R. Gilbert, R. Legtenberg, and S. D. Senturia, "3D coupled electromechanics for MEMS: applications of CoSolve-EM," in *Proc. IEEE MEMS*, 1995, pp. 122–127.

[16] F. Shi, P. Ramesh, and S. Mukherjee, "Simulation methods for micro-electro-mechanical structures (MEMS) with application to a microtweezer," *Comput. Struct.*, vol. 56, pp. 769–783, 1995.

[17] N. R. Aluru and J. White, "An efficient numerical technique for electromechanical simulation of complicated microelectromechanical structures," *Sens. Actuators A, Phys.*, vol. 58, pp. 1–11, 1997.

[18] F. Shi, P. Ramesh, and S. Mukherjee, "Dynamic analysis of micro-electro-mechanical systems," *Int. J. Numer. Methods Eng.*, vol. 39, pp. 4119–4139, 1996.
[19] R. F. Harrington, *Field Computation by Moment Methods*. Piscataway, NJ: IEEE , 1993.
[20] Z. Bao and S. Mukherjee, "Electrostatic BEM for MEMS with thin conducting plates and shells," *Eng. Anal. Bound. Elem.*, vol. 28, pp. 1427–1435, 2004.
[21] ——, "Electrostatic BEM for MEMS with thin beams," *Commun. Numer. Methods Eng.*, vol. 21, pp. 297–312, 2005.
[22] S. W. Chuyan, Y. S. Liao, and J. T. Chen, "Computational study of the effect of finger width and aspect ratios for the electrostatic levitating force of MEMS combdrive," *J. Microelectromech. Syst.*, vol. 14, pp. 305–312, 2005.
[23] G. Li and N. R. Aluru, "A Lagrangian approach for electrostatic analysis of deformable conductors," *J. Microelectromech. Syst.*, vol. 11, pp. 245–254, 2002.
[24] V. Shrivastava, N. R. Aluru, and S. Mukherjee, "Numerical analysis of 3D electrostatics of deformable conductors using a Lagrangian approach," *Eng. Anal. Bound. Elem.*, vol. 28, pp. 583–591, 2004.
[25] G. Li and N. R. Aluru, "Efficient mixed-domain analysis of electrostatic MEMS," *IEEE Trans. Comput.-Aided Des. Integr. Circuits Syst.*, vol. 22, pp. 1228–1242, 2003.
[26] S. K. De and N. R. Aluru, "Full-Lagrangian schemes for dynamic analysis of electrostatic MEMS," *J. Microelectromech. Syst.*, vol. 13, pp. 737–758, 2004.
[27] S. Mukherjee, Z. Bao, M. Roman, and N. Aubry, "Nonlinear mechanics of MEMS plates with a total Lagrangian approach," *Comp. Struc.*, vol. 83, pp. 758–768, 2005.
[28] S. Mukherjee, S. Telukunta, and Y. X. Mukherjee, "BEM modeling of damping forces on MEMS with thin plates," *Eng. Anal. Bound. Elem.*, vol. 29, pp. 1000–1007, 2005.
[29] S. Mukherjee, "On boundary integral equations for cracked and for thin bodies," *Math. Mech. Solids*, vol. 6, pp. 47–64, 2001.
[30] ——, "Finite parts of singular and hyper singular integrals with irregular boundary source points," *Eng. Anal. Bound. Elem.*, vol. 24, pp. 767–776, 2000.
[31] ——, "CPV and HFP integrals and their applications in the boundary element method," *Int. J. Solids Structures*, vol. 37, pp. 6623–6634, 2000.
[32] E. J. Nanson, "Note on hydrodynamics," *Messenger of Math.* , vol. 7, pp. 182–183, 1877–1878.
[33] S. Mukherjee, M. K. Chati, and X. Shi, "Evaluation of nearly singular integrals in boundary element contour and node methods for three-dimensional linear elasticity," *Int. J. Solids Structures*, vol. 37, pp. 7633–7654, 2000.
[34] A. H. Nayfeh and D. T. Mook, *Nonlinear Oscillations*. New York: Wiley, 1979.
[35] W. Han and M. Petyt, "Geometrically nonlinear vibration analysis of thin rectangular plates using the hierarchical finite element method—I: the fundamental mode of isotropic plates," *Comp. Struc.*, vol. 63, pp. 295–308, 1997.
[36] A. C. Ugural, *Stresses in Plates and Shells*, 2nd ed. New York: McGraw-Hill, 1999.
[37] G. B. Thomas and R. L. Finney, *Calculus and Analytic Geometry Alternate ed.* Reading, MA: Addison Wesley, 2003.
[38] A. Nagarajan and S. Mukherjee, "A mapping method for numerical evaluation of two-dimensional integrals with 1/r singularity," *Comp. Mech.*, vol. 12, pp. 19–26, 1993.
[39] M. K. Chati and S. Mukherjee, "The boundary node method for three-dimensional problems in potential theory," *Int. J. Numer. Methods Eng.*, vol. 47, pp. 1523–1547, 2000.
[40] K. E. Petersen, "Silicon as a mechanical material," *Proc. IEEE*, vol. 70, pp. 420–455, 1982.
[41] W. N. Sharpe, Jr., "Mechanical properties of MEMS materials," in *The MEMS Handbook*. Boca Raton, FL: CRC, 2001, ch. 3, pp. 3–33.
[42] S. D. Senturia, *Microsystem Design*. Boston, MA: Kluwer Academic, 2001.
[43] M. I. Younis, E. M. Abdel-Rahman, and A. Nayfeh, "A reduced order model for electrically actuated microbeam based MEMS," *J. Microelectromech. Syst.*, vol. 12, pp. 672–680, 2003.

Srinivas Telukunta (S'05) received the B.Tech. degree in aerospace engineering from the Indian Institute of Technology, Madras, in 2000 and the M.S. and Ph.D. degrees in mechanical engineering from Cornell University, Ithaca, NY, in 2003 and 2005, respectively. His thesis included work on the analysis and design of electrostatic MEMS.

Currently, he leads the design and simulation effort at Pixtronix Inc, a startup based in Boston, MA which provides MEMS based displays for portable electronics industry. Prior to this, he worked as a process development engineer with Binoptics Inc, a startup company based in Ithaca, NY, which provides integrated optoelectronic components using proprietary "Etch Facet Technology (EFT)".

Dr. Telukunta is a Student Member of the American Society of Mechanical Engineers (ASME).

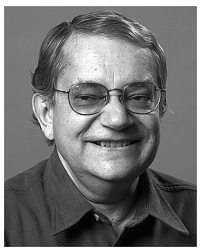

Subrata Mukherjee received the B.S. degree in mechanical engineering from the Indian Institute of Technology, Kharagpur, in 1967 and the Ph.D. degree in applied mechanics from Stanford University, Stanford, CA, in 1972.

He joined the Cornell faculty in 1974. Since then, he has been a Visiting Faculty Member at the University of Waterloo, Waterloo, ON, Canada, at the Technische Hochschule in Darmstadt, Germany, at the University of Arizona, Tucson, and at the Ecole Polytechnique in Palaiseau, France. He has authored or coauthored three books, edited two books, written eleven invited review articles and over one hundred and seventy articles in archival journals, mostly in the area of computational solid mechanics. Over the years, he has supervised 25 completed Ph.Ds. His primary field of research is computational mechanics, with emphasis on applications of the boundary element and related mesh-free methods in solid mechanics, shape optimization problems and micro and nano-electromechanical systems (MEMS and NEMS).

Dr. Mukherjee is a Fellow of the American Society of Mechanical Engineers (ASME) and of the American Academy of Mechanics and a Member of several other professional societies. He is an Associate Editor of the *ASME Journal of Applied Mechanics*.